LASER INTERFEROMETER GRAVITATIONAL WAVE OBSERVATORY
- LIGO -
CALIFORNIA INSTITUTE OF TECHNOLOGY
MASSACHUSETTS INSTITUTE OF TECHNOLOGY

Technical Note	**LIGO-T1800224–v0**	2018/09/28

Physical and Statistical Analysis of Scatter in Fabry-Pérot Arm Cavity of Advanced LIGO

Wenxuan Jia
Mentor: Anamaria Effler, Valery Frolov

California Institute of Technology
LIGO Project, MS 18-34
Pasadena, CA 91125
Phone (626) 395-2129
Fax (626) 304-9834
E-mail: info@ligo.caltech.edu

Massachusetts Institute of Technology
LIGO Project, Room NW22-295
Cambridge, MA 02139
Phone (617) 253-4824
Fax (617) 253-7014
E-mail: info@ligo.mit.edu

LIGO Hanford Observatory
Route 10, Mile Marker 2
Richland, WA 99352
Phone (509) 372-8106
Fax (509) 372-8137
E-mail: info@ligo.caltech.edu

LIGO Livingston Observatory
19100 LIGO Lane
Livingston, LA 70754
Phone (225) 686-3100
Fax (225) 686-7189
E-mail: info@ligo.caltech.edu

http://www.ligo.caltech.edu/

Abstract

In the dual-recycled Michelson interferometer of Advanced LIGO, the optical scatter exists in the resonant Fabry-Pérot arm cavities due to imperfections of test mass surfaces. We studied scatter in Observation Run 2 with measurements of photo diodes on the arm cavity baffle, and investigated its relation with other factors sampled from auxiliary data channels. The steady-state scatter during locks of interferometer is analyzed and compared with FFT-based simulation. Regression analysis is carried out to find the correlation between beam position and transient scatter measurements, when the main beam moves on the test masses by the alignment system before each lock. With the ensemble regression model, the beam position on test mass can be inferred from scatter distribution on baffle with $\sigma < 0.5$ mm and cross-calibrated with dither-based methods. The scatter with the new end test mass installed are predicted for the upcoming Observation Run 3.

Contents

1 Introduction

The Laser Interferometer Gravitational-wave Observatory (LIGO) is a complex system of instruments designed to detect the gravitational wave (GW) by interferometry of coherent monochromatic light. According to Einstein's theory of general relativity, gravitational wave can be understood as a propagating disturbance of space-time fabric caused by catastrophic astrophysical events, for example, the merging of a pair of black holes or neutron stars. Such disturbance would cause a strain in space on the scale of 10^{-21}, an incredibly small quantity to measure directly. Therefore, Michelson interferometry with power and signal-recycling cavities shown in Figure 1 is employed in Advanced LIGO (aLIGO) to pursue the detection of the infinitesimal strain.

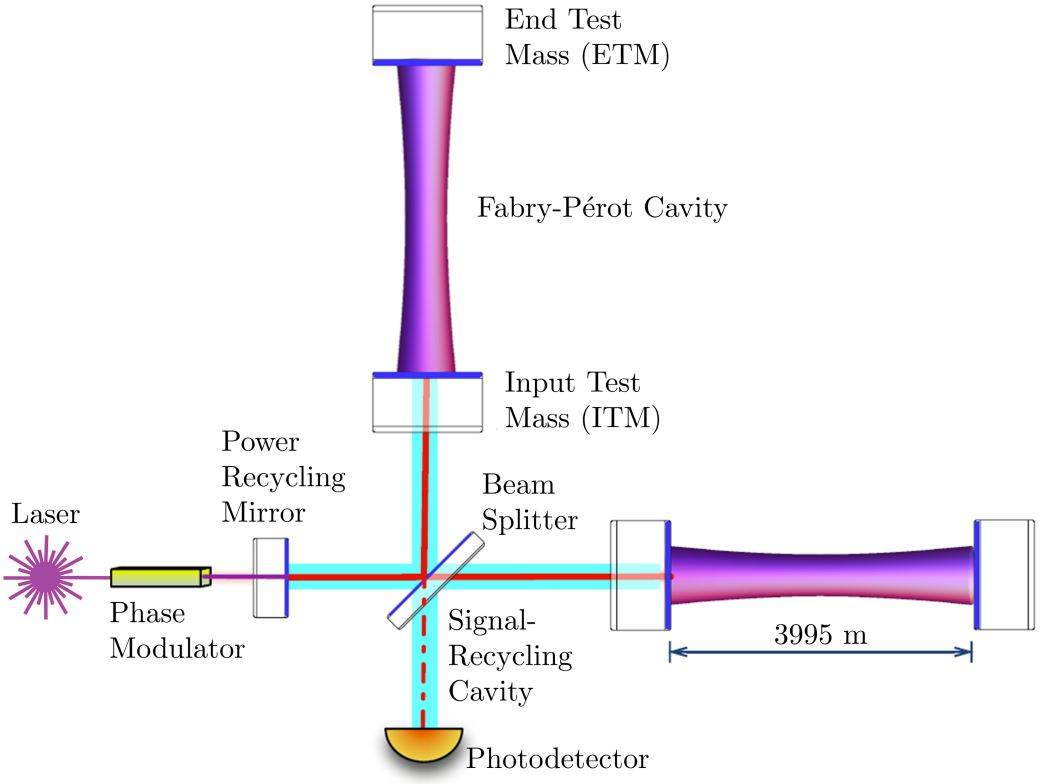

Figure 1: Simple schematics of LIGO core optics [1].

As GW sweeps through the interferometer, it stretches the length of one arm and shrinks that of the other arm, and the phase change of the light stored in the arm cavities is accumulated and detected by the photodetector [2]. To elongate the detector's interaction time with GW, its optical path length is increased by folding the interferometer arms with the Fabry-Pérot (FP) technique. The FP cavity is essentially composed of two highly-reflective plane mirrors facing towards each other, separated by a distance in multiples of half of the wavelength (see Appendix A for more detail). In Observation Run 2 (O2) from 11/30/2016 to 08/25/2017, the laser power stored in the arm cavity was increased to 110 kW to reduce the quantum noise and enhance the sensitivity in high frequency range. As the result, the scattered light due to the imperfection of the test mass mirrors intensified correspondingly, introducing noises to

the detector. Thus, it is necessary to quantify and analyze the scatter through photodiode measurements on the time scale of entire O2. The change of the test mass surface quality and other components of core optics can be inferred from the long-term scatter.

Previous analysis of scatter in FP arm cavity includes Rew's work and Yamamoto's Static Interferometer Simulation (SIS). Rew *et al.* used Bi-directional Reflectance Distribution Function (BRDF) to characterize scatter measurements from 05/2014 to 08/2014 [3]. However, his scatter data fluctuated with uncertainties too large to analyze because the detector was not in the low-noise observing mode. In O2, there were more repeatable locks for a longer period of time, so it is possible to observe a trend of change of scatter under controlled conditions. To understand the physics of scatter, Yamamoto created a FFT-based simulation tool that computes field propagation in the resonant cavity based on user-defined high-reflective (HR) profiles of the test masses [4]. It mainly takes the measured phase map of the coated surface and convolute it with paraxial diffraction kernel to find the power distribution at certain location. It will be interesting to compare the simulated result with actual measurements of scatter. Since the scatter is rather an inevitable phenomenon, we seek to take advantage of it and extract useful information from its measurements. In this project, we aim at understanding the data measurements of scatter and exploring applications with such information. Various types of regression analyses are done on the couplings between scatter and other physical quantities of LIGO Livingston Observatory (LLO) in Observation Run 2, for example the main beam position and time, to provide fundamentals for future investigations.

The rest of the paper is organized in sections with different theme of analysis. Section 2 characterizes the steady-state scatter measured during locks of resonant cavity and compares it with SIS result. The longest period when the beam position was fixed is selected to analyze the long-term change of steady-state scatter. Section 3 discusses about the transient scatter when the main beam is aligned to the lock position. The changes of scatter along the beam alignment paths are analyzed. In Section 4, various parametric regression models are explored to predict the beam position from scatter distribution. The paper is concluded in Section 5 with prediction of scatter under the new test mass for Observation Run 3.

2 Steady-state Scatter

2.1 Scatter characterization & measurement

Optical scatter is a phenomenon when small amount of photon does not follow the designed path after interacting with optics, usually caused by the unevenness of the surfaces of optics. In aLIGO, a pair of test mass mirrors made of fused silica form the 4-km long FP cavity of single arm. To achieve the desired finesse of the cavity, the 34-cm diameter test mass is coated with layers of high-reflective materials as shown in Figure 2. Although the coating roughness is on the scale of a few nanometers, it still causes scatter in the order of 10^{-4} W under 110 kW of laser power in the FP cavity, especially the end test mass in both of arms. The fact that the coating surface of ETM with higher PSD in Figure 2 (c) results in more scatter from ETM would be revealed in the simulation.

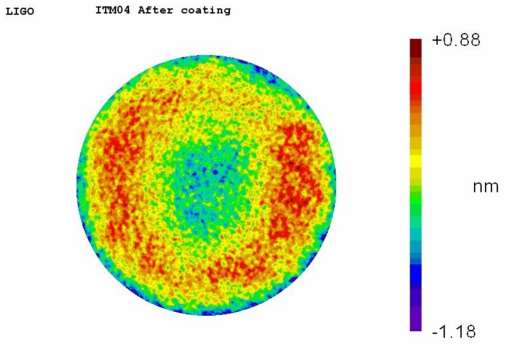

(a) ITMX coating measurements[5]

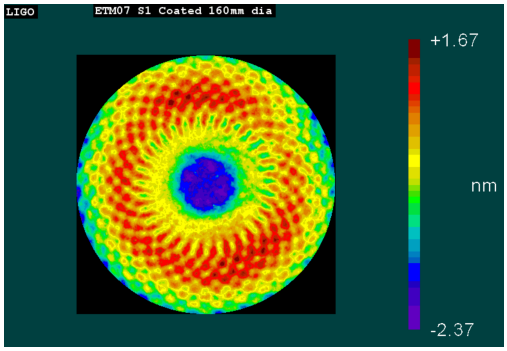

(b) ETMX coating measurements[6]

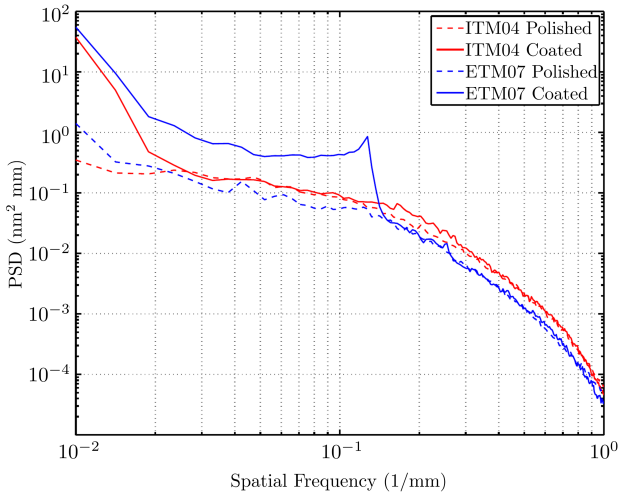

(c) Power spectral density (PSD) of the phase map of polished/coated ITMX/ETMX [7]

Figure 2: Figure measurements of (a) ITMX (ITM04) and (b) ETMX (ETM07) of LLO in O2 (credit: GariLynn Billingsley). The coating quality of two test masses are shown in (c). Note the PSD of ETM07 coated is higher than others. The situation is similar in Y-arm.

The BRDF is a common function used to characterize scatter in many disciplines such as optics and computer graphics. The general definition of BRDF is the differential of outgoing radiance with respect to the incoming irradiance incident on the surface. For the scatter on test masses, the incoming irradiance is the power stored in FP cavity, and the BRDF can be modeled in Figure 3 and Equation 1 [3].

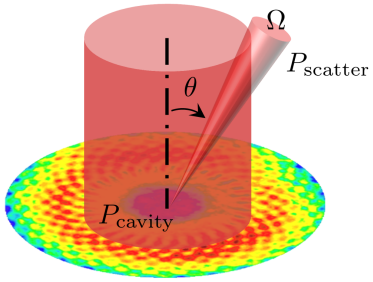

Figure 3: Schematics of scatter from the test mass HR profile. The red cylinder is the main beam and the colorful disk resembles ETMX surface aberration in Figure 2 (b).

$$\text{BRDF}(\theta) = \frac{P_{\text{scatter}}}{P_{\text{cavity}} \Omega \cos\theta} \tag{1}$$

where P_{scatter} is the power of scatter measured at solid angle Ω with zenith angle θ. It is a normalization of scatter with respect to the total incident power and the solid angle of measurements. We will use BRDF extensively to quantify scatter.

To prevent scattered photons with noisy phase from re-entering the main beam of interferometer, multiple light baffles are mounted on beam paths as shown in Figure 4.

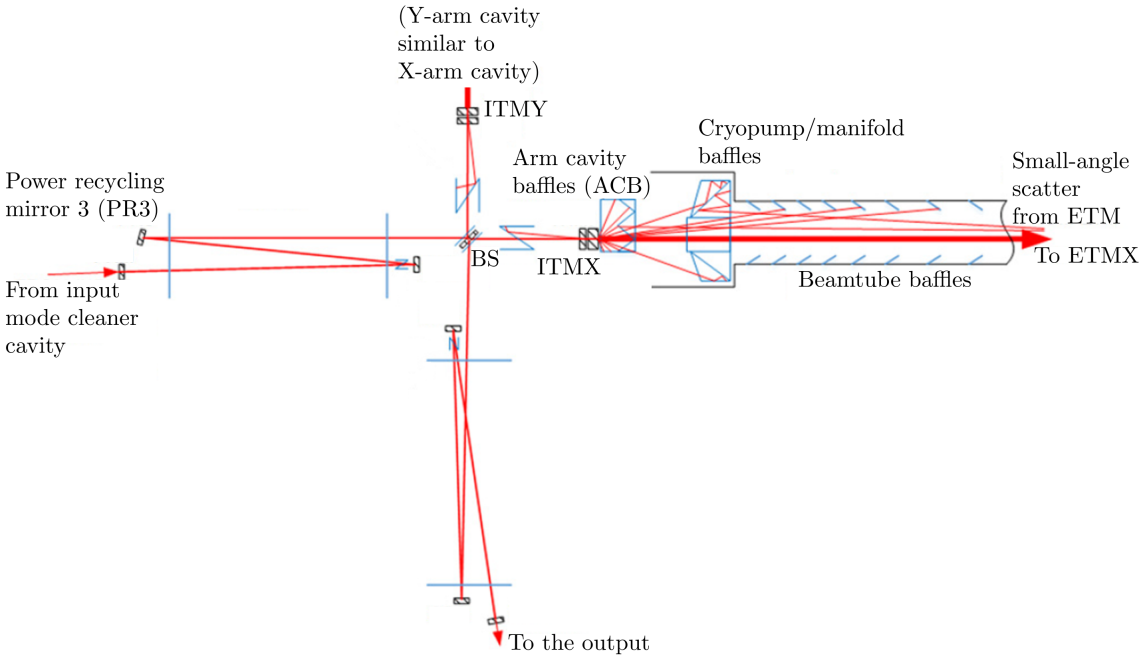

Figure 4: Locations of scattered light baffles in the LIGO optical configuration [7].

Those beamtube baffles mounted on the sidewalls of the ultra-high vacuum cavity as well as the cryopump/manifold baffles are meant to block the large-angle scatter. The small-angle scatter from the far test mass (4 km away) is caught by the arm cavity baffle (abbreviated as baffle) placed in front of each test mass optic [7]. There are four *Excelitas YAG-444-AH* photo diodes (PD) mounted on each baffle of the test mass to measure the intensity of small-angle scattered light from the test mass on the other side of FP cavity. The configurations of PD are pictured in Figure 5, and the calibration equation of PD is given as Equation 2:

$$P = \frac{V}{RTG} \tag{2}$$

where P is the power derived from measured voltage V, responsivity R (0.47 A/W), transimpedance T (20 kΩ) [8] and analog gain G of 1.

In O2, all of the 16 PDs mounted on 4 baffles have measured the scatter intensity with sampling frequency of 16 Hz, and the raw voltage data can be accessed via channels *L1:AOS-I(E)TMX(Y)_BAFFLEPD_1(2,3,4)_VOLTS*. The variance across PD 1 and 4 on the same baffle are calibrated to ensure valid comparison of scatter power measured by them (see Appendix B).

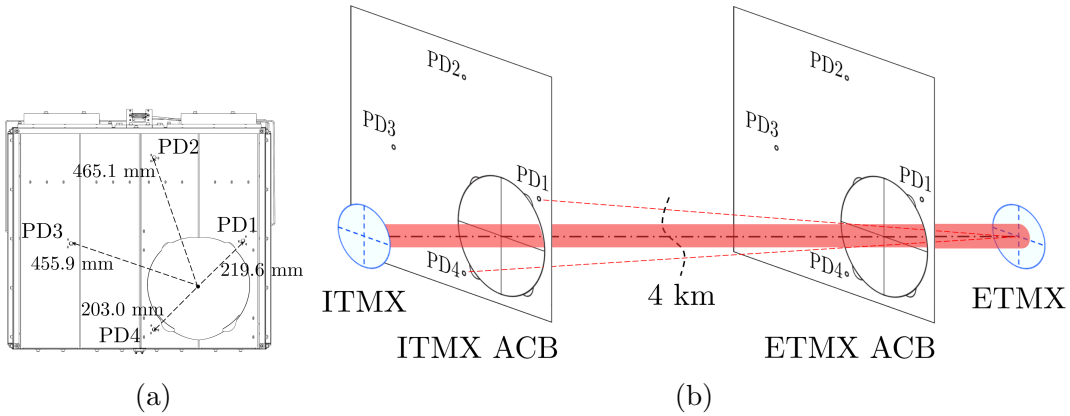

Figure 5: Schematics of the baffle PD measuring small-angle scatter. (a) the front view of the baffle with four PD mounted (Note that PD 1 and 4 are closer to the aperture than PD 2 and 3 [9]). (b) FP cavity with sample ETMX scatter caught on ITMX baffle PD 1 and 4. The shaded line is resonant main beam and the scatter paths are annotated in dashed lines. The configuration in Y-arm is symmetrical with respect to the diagonal of two orthogonal arms.

2.2 Static interferometer simulation (SIS)

Given the phase map of the test mass, its diffraction can be obtained from Huygen's Principle. The problem is set up in Figure 6.

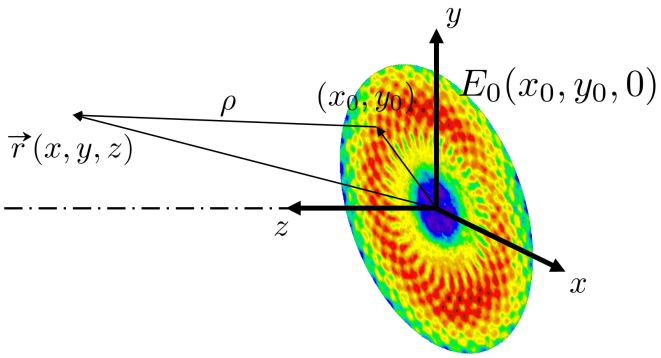

Figure 6: Set-up of computation of field amplitude at position $\vec{r}(x, y, z)$ from ETMX surface. The point (x_0, y_0) refers to location on the uneven profile.

Each point (x_0, y_0) on the test mass serves as a source of spherical wavelet, whose phase shift is contained in the complex field $E_0(x_0, y_0, 0)$. The field at point (x, y, z) can be computed by Equation 3.

$$E(\vec{r}) = \frac{i}{\lambda} \iint_{map} dx_0 dy_0 E_0(x_0, y_0) \frac{e^{-ik\rho} z}{\rho^2} \tag{3}$$

where $\lambda = 1064$ nm is the wavelength and $\rho = \sqrt{(x - x_0)^2 + (y - y_0)^2 + z^2}$. With Fresnel

approximation for $z \gg x, y$, a few simplifications can be made:

$$\rho \approx z\left(1 + \frac{(x-x_0)^2 + (y-y_0)^2}{2z^2}\right) \tag{4}$$

and

$$\begin{aligned} E(\vec{r}) &= \frac{i}{\lambda}\iint_{map} dx_0 dy_0 E_0(x_0, y_0)\frac{e^{-ikz}}{z}e^{-ik\left((x-x_0)^2+(y-y_0)^2\right)/(2L)} \\ &= \frac{ie^{-ikz}}{\lambda z}\iint_{map} dx_0 dy_0 E_0(x_0, y_0)e^{-ik\left((x-x_0)^2+(y-y_0)^2\right)/(2L)} \end{aligned} \tag{5}$$

Since the optics in space can be understood as a space-invariant linear system, the computation of the convolution in Equation 5 can be greatly simplified by 2-D Fourier transformation [10]. Denote the transformed variable with a tilde, the original field E_0 can be represented as

$$\tilde{E}_0(f_x, f_y) = \iint E_0(x, y)e^{-i2\pi(f_x x + f_y y)}\,dx\,dy \tag{6}$$

and the transformed field at $\vec{r}$ is simply

$$\tilde{E}(\vec{r}) = \tilde{E}_0 \cdot \tilde{K} \tag{7}$$

where $\tilde{K}$ is the paraxial diffraction kernel computed by 2-D transforming the rest of the convoluted function:

$$\tilde{K}(f_x, f_y) = \frac{ie^{-ikz}}{\lambda z}\iint e^{-ik\left(x^2+y^2\right)/(2L)}e^{-i2\pi(f_x x + f_y y)}\,dx\,dy \tag{8}$$

This formalism constitutes the basics of the SIS simulation, which offers much more customization of parameters of optics. The implementation of SIS is summarized in Figure 7.

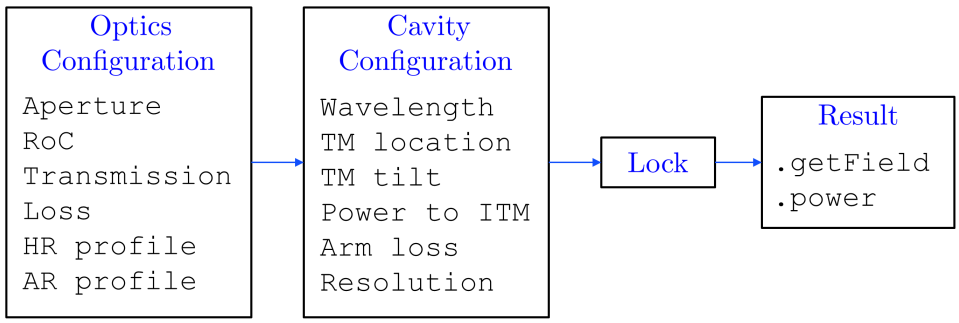

Figure 7: Workflow of the static interferometer simulation.

The simulated BRDF profile in the X-arm of LLO is shown in Figure 8. Since the coatings of ETM in both arms reveal a stronger PSD in Figure 2, the spiral pattern is only visible on ITM baffles.

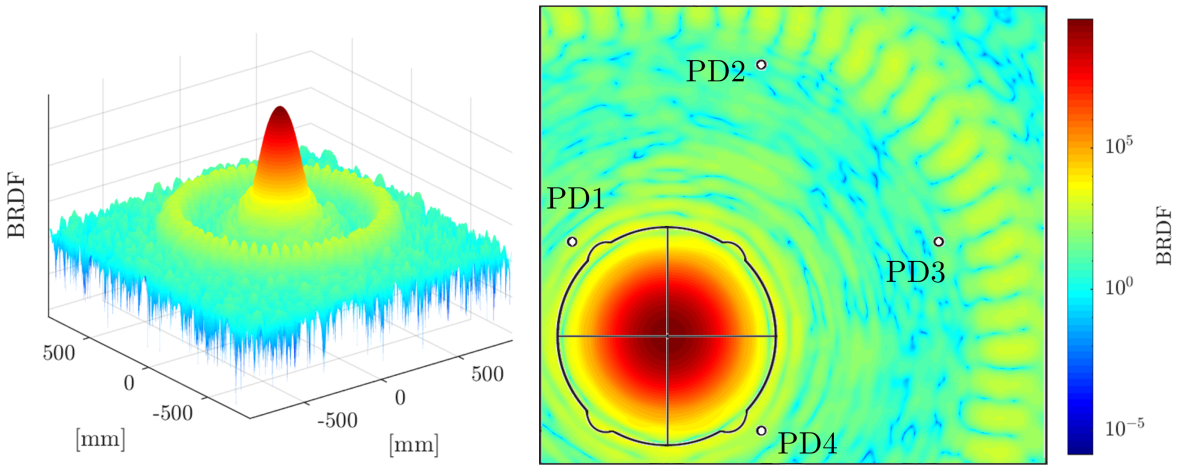

(a) Scatter on ITMX baffle from ETMX.

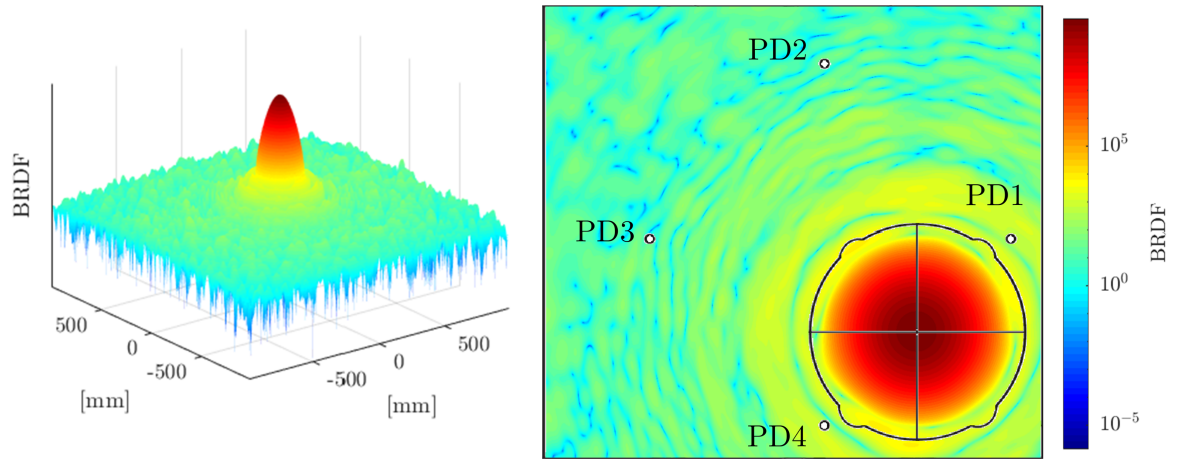

(b) Scatter on ETMX baffle from ITMX.

Figure 8: Field intensity profile viewed from 3-D and on the baffle of (a) ITMX and (b) ETMX. The PD 1 and 4 are on the airy ring caused by diffraction from mirror edges. PD 2 and 3 on ITMX are next to the spiral pattern caused by uneven coating. The simulation of Y-arm is similar.

In addition to the diffraction of the phase map bumps, the edge of the test mass should also be accounted as a source of diffraction in a realistic FP cavity. The simulations for three different cases where the cavity is ideal, the test mass is finite but perfectly smooth and actual cavity in aLIGO are represented in Figure 9. Gaussian beam profile is seen in the range of the aperture on baffle, and the bump at 500-600 mm radial distance in the phasemap curve of ITMX corresponds to the spiral pattern. The phasemap case differs from finiteness case for around an order of magnitude at radial distance large than 200 mm, and differs from nominal case for multiple orders of magnitude. The measurement of actual scatter is expected to match most with the phasemap curve.

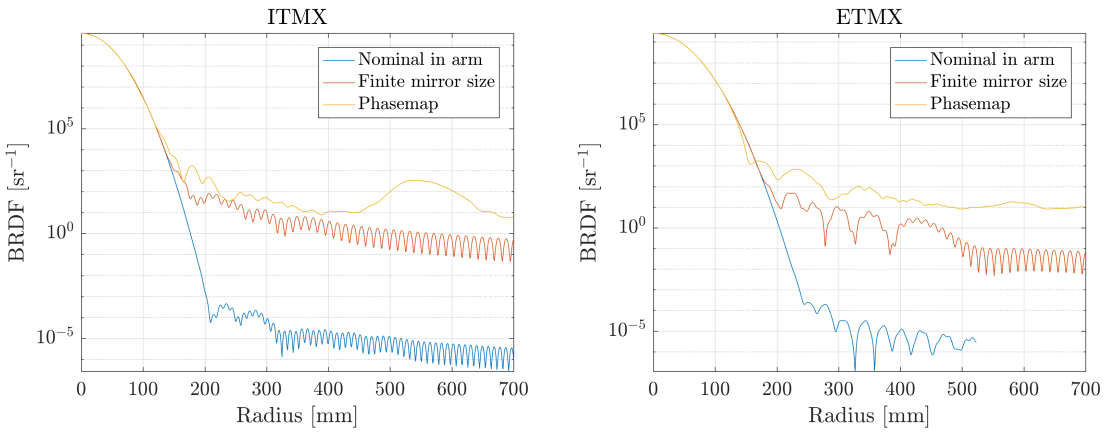

Figure 9: Comparison of radially integrated 2-D BRDF profiles on ITMX and ETMX baffle under three different circumstances. The radius is the radial distance from the center of the main beam on baffle.

2.3 Scatter change through Observation Run 2

The dual-recycled Michelson interferometer is most sensitive to gravitational ripples in space-time when all of its cavities are locked in resonance. However, various external factors caused the detector to fail maintaining the desired locked state in O2, during which the PD was not measuring the steady-state scatter of the full power of the main beam. Even in the low-noise mode, the interferometer may be under other tests instead of observing GW. These periods are not interesting to us, and we remove the PD data in these disturbed time intervals. In addition, the scatter is also susceptible to changes in the beam positions caused by pitching or yawing the test mass. Therefore, the PD data needs to be filtered such that they are only measuring the scatter during stable observing periods (science-run mode). Table 1 summarizes known factors that affect scatter in O2 and their channel names.

Table 1: Known factors that couple with small-angle scatter in FP cavity

Factors	**Channel names**
Locked state	*L1:GRD-ISC_LOCK_STATE_N*
Science-run mode	*L1:ODC-OPERATOR_OBSERVATION_READY*
Power in recycling cavity	*L1:IMC-PWR_IN_OUTPUT*
Test mass attitude	*L1:SUS-I(E)TMX(Y)_L2_DRIVEALIGN_P(Y)2L_GAIN*

For each locked state, its transient response is filtered by removing the first and last 1 hour of data in its period, when the thermal transient effect occurs. The transience filter of 1 hour is also applied to periods when all *DRIVEALIGN* gains are constant. The resulting PD data through entire O2 is presented in Figure 10.

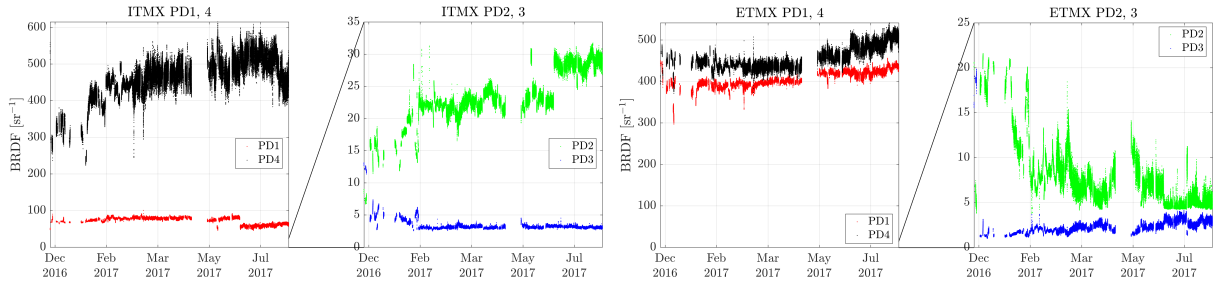

(a) ITMX PD (b) ETMX PD

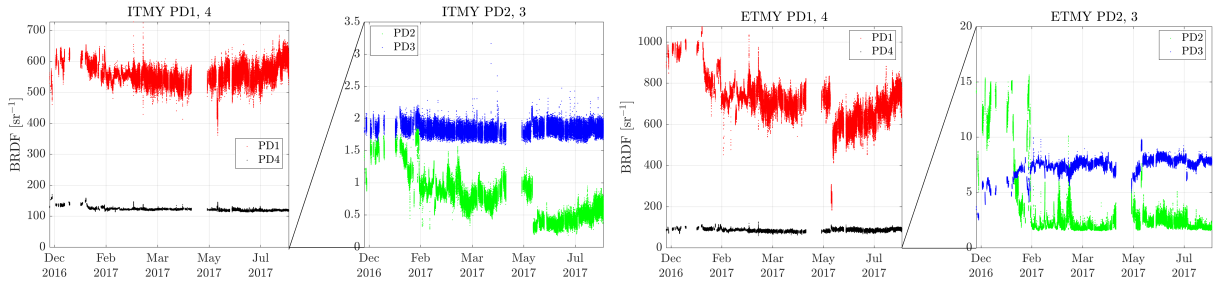

(c) ITMY PD (d) ETMY PD

Figure 10: Filtered PD minute-trend data on all arm cavity baffles throughout O2. The color red, green, blue, black (RGBK) represent PD 1-4 respectively.

Since the PD 1 and 4 are closer to the main beam than PD 2 and 3, they receive higher scatter intensity. The entire minute-trend data of O2 is stable within a factor of 2, except for ETMX and ETMY PD 2. The reason for the large variation of PD 2 before February 2017 is unknown. The beam spot position setting of PR2 remains constant for all the filtered periods of O2, thus its coupling with scatter can be ignored. The total eight yaw & pitch gains for four test masses are constant only for certain period in the O2, which implies that the beam positions in locks were not always the same. The variation of beam position was at most 5 mm throughout O2. The data is sectioned according to locks so that all test masses are fixed in the period of single section. A total of 381 sections are found in O2 when the following criteria are satisfied simultaneously:

1. The cavity is locked for more than 3 hours (first and last 1 hour transience are filtered)
2. All yaw & pitch gains are constant for more than 3 hours (transience will be filtered)
3. The variation of laser power input is less than 1 W

The periods of constant beam positions are summarized in Table 2

Table 2: Stable beam positions in O2. The start date for each row of position (in mm) is in the leftmost column of that row. The coordinate system is from the point of view of the other test mass, and y is always vertically up to the ground.

	ITMX_x	ITMX_y	ETMX_x	ETMX_y	ITMY_x	ITMY_y	ETMY_x	ETMY_y
02-Dec-2016:	-6.21	3.50	2.10	-2.80	1.46	2.60	-0.35	-4.15
07-Dec-2016:	-6.21	3.50	-1.75	-2.80	1.46	2.60	-0.35	-4.15
15-Dec-2016:	-6.21	3.50	-3.50	-2.80	1.46	2.60	-0.35	-4.15
15-Dec-2016:	-6.21	3.50	-1.75	-2.80	1.46	2.60	-0.35	-4.15
24-Jan-2017:	-7.64	3.73	-1.75	-2.80	2.54	2.82	-0.35	-4.15
17-Feb-2017:	-7.30	3.73	-1.75	-2.80	2.55	2.82	-0.35	-4.15
25-Feb-2017:	-7.30	3.73	-1.75	-2.80	1.46	2.60	-0.35	-4.15
06-Jun-2017:	-7.30	3.73	-1.75	0.35	1.46	2.60	-0.35	0.35
08-Jun-2017:	-7.30	3.73	-1.75	-2.80	1.46	2.60	-0.35	-2.80
02-Jul-2017:	-7.30	3.73	-1.75	0.35	1.46	2.60	-0.35	-2.80
02-Aug-2017:	-6.21	3.73	-1.75	0.35	1.46	4.40	-0.35	-2.80
03-Aug-2017:	-7.30	3.73	-1.75	0.35	1.46	4.40	-0.35	-2.80
04-Aug-2017:	-7.30	3.73	-1.75	0.35	1.46	2.60	-0.35	-2.80

It is seen that the longest period in Table 2 is from 02/24/2017 to 06/08/2017, which is the longest duration of controlled beam position. Therefore, the time series of PD data are obtained for all locks in this period, whose average and uncertainty (standard deviation) are computed and presented in Figure 11.

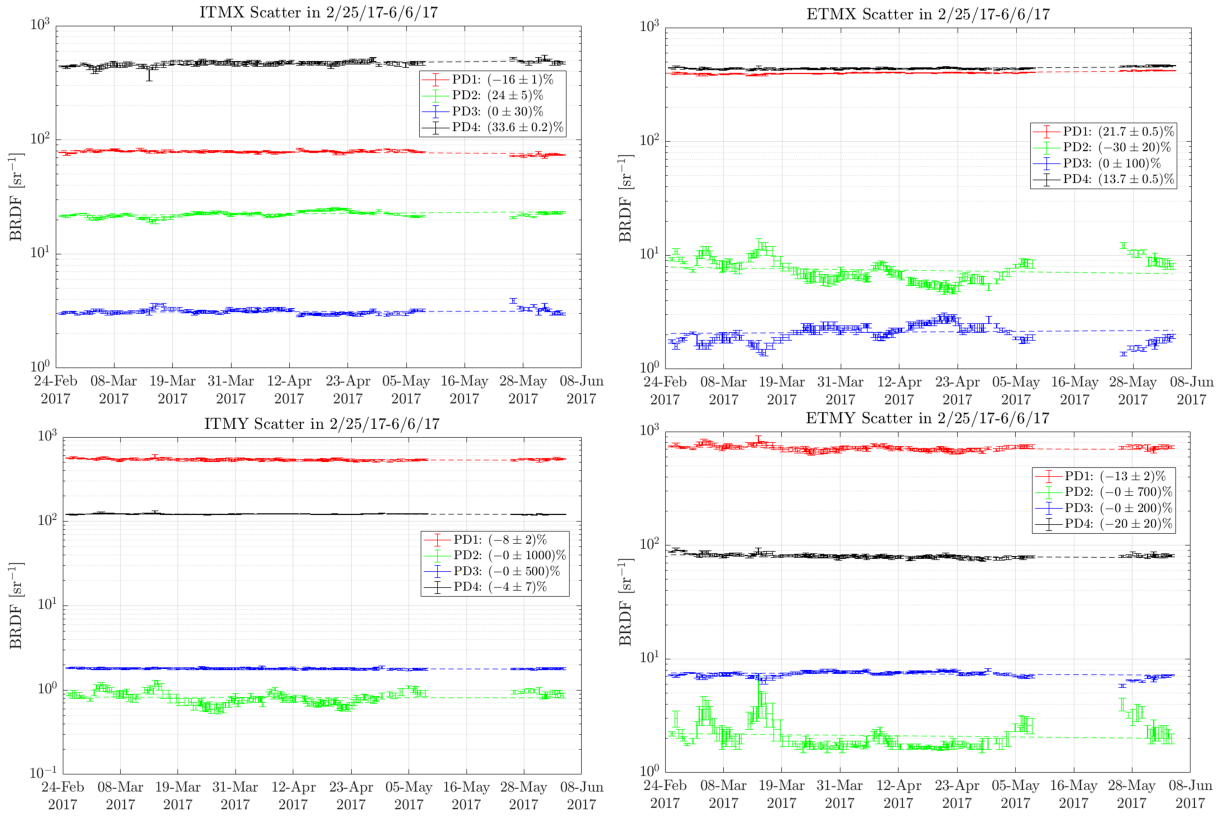

Figure 11: Trend of scatter measured on all sections from the longest stable duration.

Line fitting is done on each trend data, and their slopes presented in the legend of each graph are used to estimate overall change of scatter power. Since the PD 2 and 3 measure

relatively small scatter, their data are more unsteady with excessive uncertainties. The rest of the trend is summarized in Table 3.

Table 3: Scatter change measured by PD 1 and 4 in the longest stable duration (02/24/17 - 06/08/17).

	ITMX	**ETMX**	**ITMY**	**ETMY**
PD 1	-16 ± 1%	21.7 ± 0.5%	-8 ± 2%	-13 ± 2%
PD 4	33.6 ± 0.2%	13.7 ± 0.5%	-4 ± 7%	-20 ± 20%

Overall, it is difficult to summarize an unified trend for these inconsistent PD measurements and conclude for scatter change over O2. There could be other factors and systematic errors affecting the measurements or scatter itself, but it is not well understood and accounted in this report.

2.4 Comparison with SIS

The scatter of each lock in O2 are compared with SIS results in Figure 12.

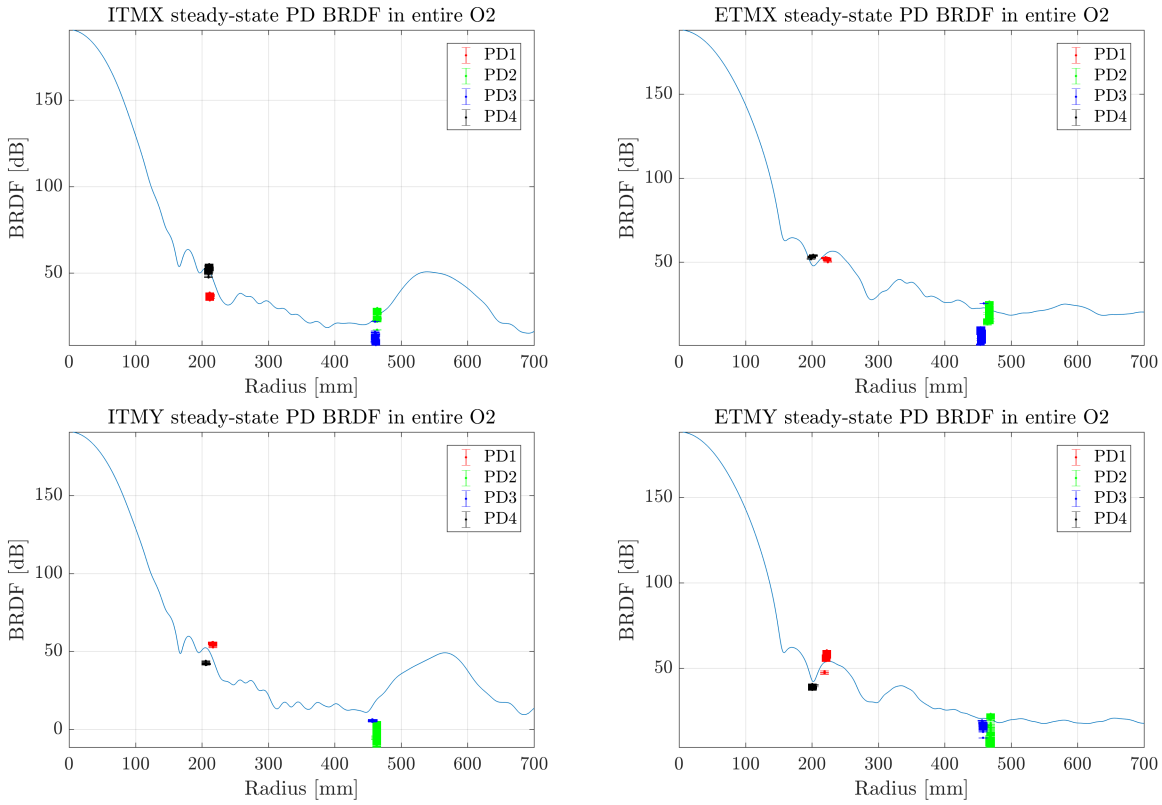

Figure 12: Comparison of the scatter measured on four baffles and simulation using centered beam position on the test mass phase map. Note that the BRDF is represented in decibel (dB) to ease determination of factor of difference.

It is seen that the measured scatter is at the same order of magnitude with the simulation prediction, demonstrating the effect of diffraction caused by finite edge of the test mass and its phase map profile (Figure 9). However, the location of PD 2 and 3 are not in the range of spiral pattern to measure its influence. Zoomed-in views at 10 mm around the radius of PD are shown in the Figure 13 for more detailed quantitative comparison.

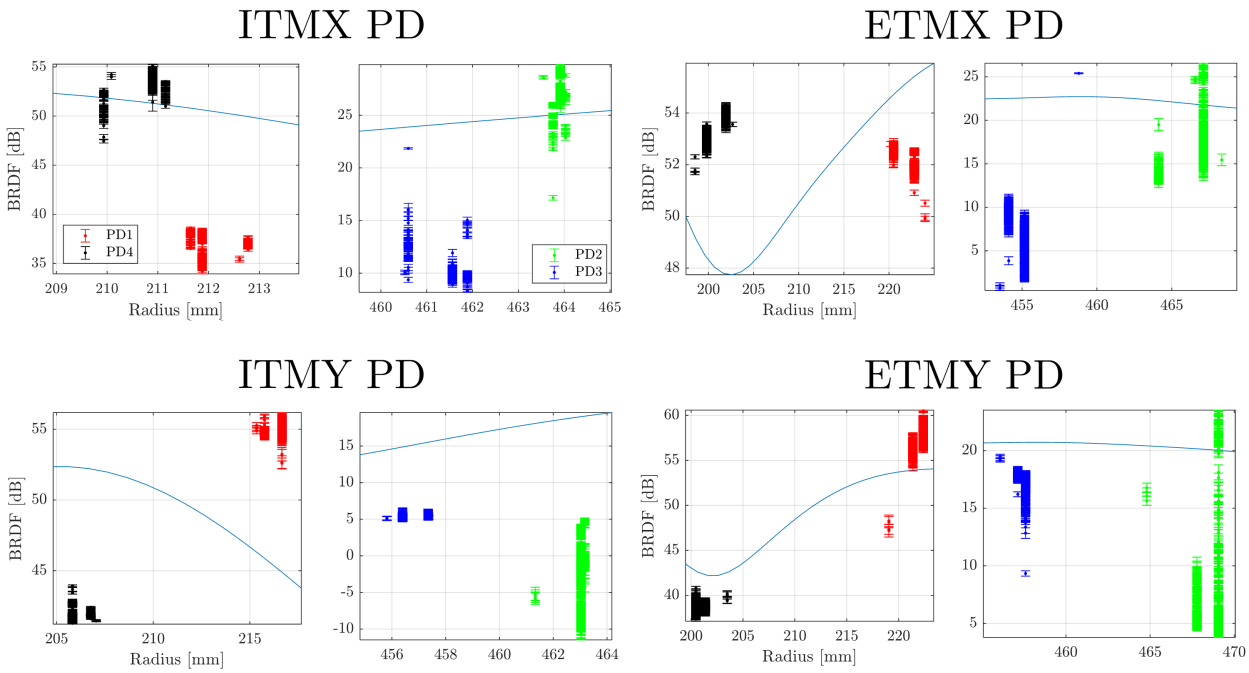

Figure 13: Comparison of simulation curve with scatter measurements of all locks in O2. Each dot with error bar represents what PD measures in one lock.

While some of the PD data are right on the curve, the maximal difference between measured data and simulation is around 10 dB (factor of 3). For the semi-quantitative simulation limited by the resolution and precision of phase map, the SIS is not able to predict scattered BRDF on a scale of a few decibel. At the same radial distance, PD 1 and 4 generally have smaller variance than PD 2 and 3, where the ETMY PD2 extends for an order of magnitude (20 dB) difference at the same radius. One may argue that the simulation profile is not the same for every pair of beam positions on ITM and ETM. However, the maximal variation among these 2-D profiles simulated under all pairs of beam position in Table 2 is within 3 dB at PD radius, which hardly explains the 10 dB difference. Given that the simulation is much simpler than reality in aLIGO, for example, the two FP cavities are coupled rather than independent like simulation, the measurements and prediction are still a good match within 10 decibels.

3 Transient Scatter

3.1 Alignment & Dither System

During O2, the test masses in the FP cavity would drift from optimal alignment and fail to form resonance. The main beam was then aligned back to the correct position by the alignment dithering system (ADS) under alignment sensing control subsystem of advanced LIGO. The ADS control system detects the beam position by dithering the end test mass at low frequency $f_{\text{dither}} < 10$ Hz, which causes a peak at f_{dither} in the amplitude spectral density of the differential arm (DARM) signal, as shown in Figure 14.

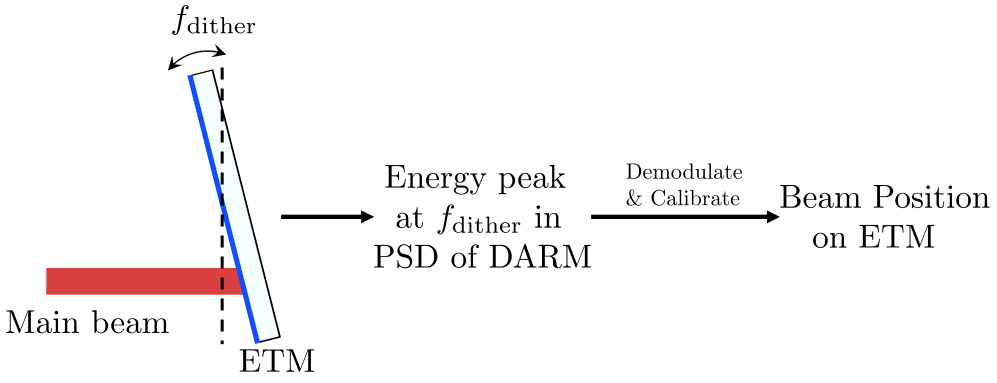

(a) Schematics of ADS system.

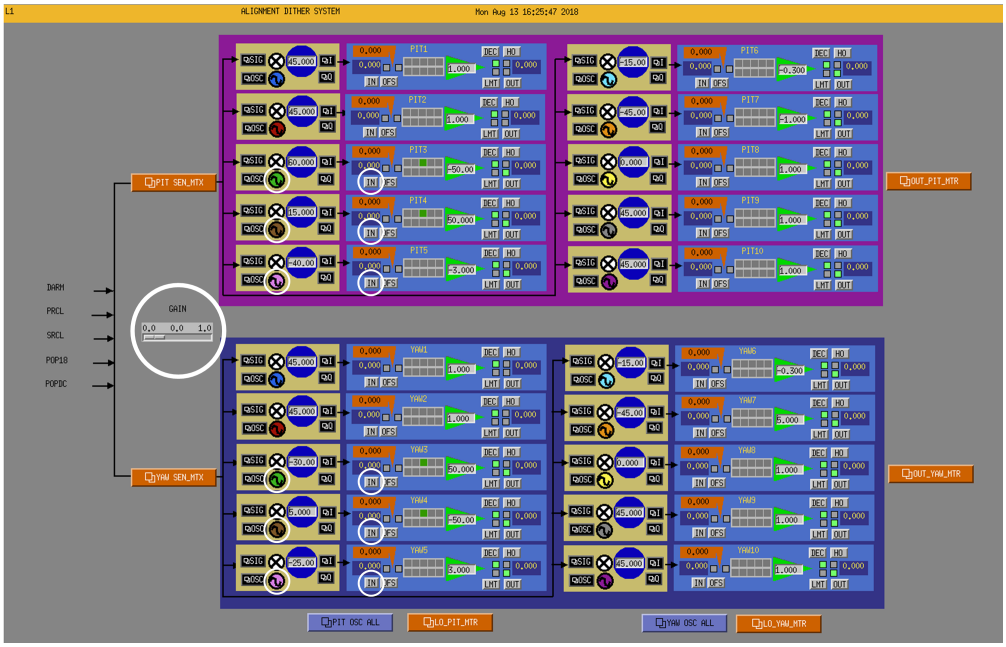

(b) LLO ADS in sitemap.

Figure 14: The alignment & Dither System (ADS) schematics (a) and sitemap (b). Channels related to this project are circled in white. The numbers of channels (3,4,5) corresponding to ETMX, ETMY and PR2 are determined by the input and output matrices in orange block.

When the beam deviates from the desired lock position specified by the feedforward pitch/yaw gains (*L1:SUS-I(E)TMX(Y)_L2_DRIVEALIGN_P(Y)2L_GAIN*), the demodulated amplitude at f_{dither} in DARM would change correspondingly. Then the control system would suppress the ADS error signal (the difference between the demodulated amplitude feedback and desired amplitude) to the steady-state zero. Thus, more beam position data points and the corresponding scatter are provided from the transient beam alignment processes. The ADS data channels are listed in Table 4.

Table 4: ADS channels along with descriptions. (* is 3 for I/ETMX, 4 for I/ETMY and 5 for PR2)

Descriptions	**Channel Names**
General feedback gain	*L1:ASC-ADS_GAIN*
Pitch dither magnitude	*L1:ASC-ADS_PIT*_OSC_CLKGAIN*
Pitch error	*L1:ASC-ADS_PIT*_DOF_INMON*
Yaw dither magnitude	*L1:ASC-ADS_YAW*_OSC_CLKGAIN*
Yaw error	*L1:ASC-ADS_YAW*_DOF_INMON*

Since the ADS error signal is proportional to both beam deviation and dithering magnitude of the end test mass as seen in Figure 14 (a), its coupling with beam position is extracted by normalizing it with respect to dithering and general feedback gain. The setting of feedforward pitch/yaw gains are not always constant for the entire O2, as seen in Table 2. Thus, we start the analysis by focusing on the longest period where all feedforward gains on test masses and PR2 stayed unchanged (2/25/17 - 6/6/17). During this period, there were 159 beam alignment process identified before each lock, when the laser power was 25 W and state number (*L1:GRD-ISC_LOCK_STATE_N*) was 1731. A sample second-trend of transient scatter in one of the beam alignment process is shown in Figure 15.

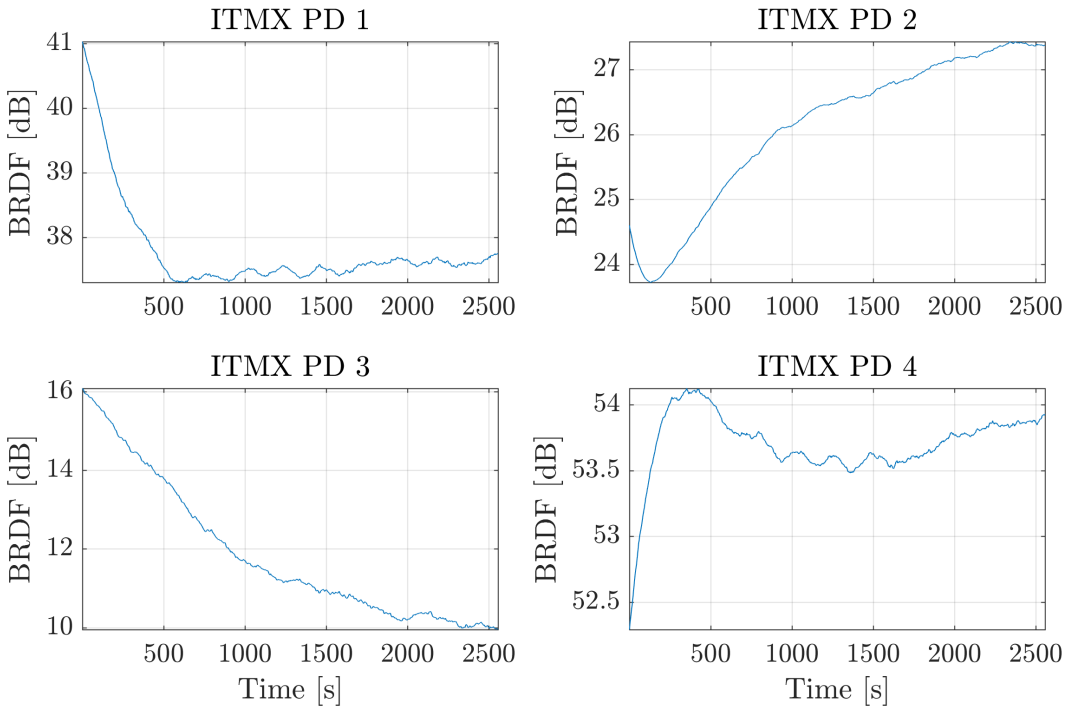

(a) ITMX PD measurements

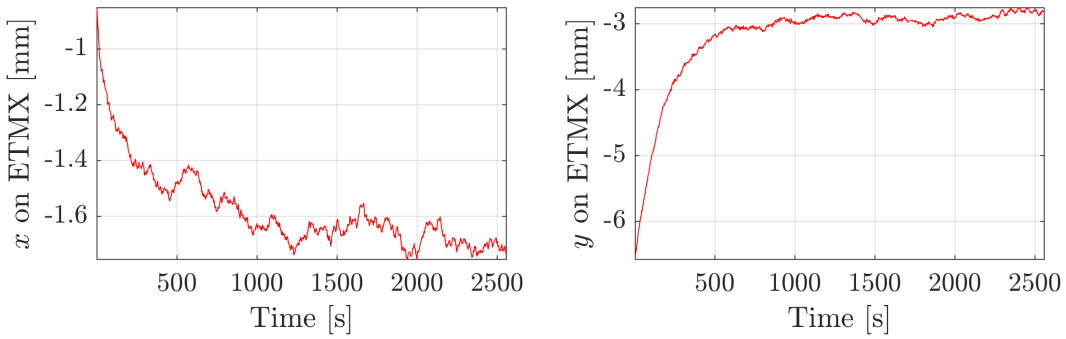

(b) ETMX beam position (view from the other test mass)

Figure 15: Responses of (a) ITMX PD measurements along with (b) beam position on 03/29/2017. The data is filtered with 120-second moving average filter to remove high frequency noise.

It is seen that the PD measurements vary for roughly 5 dB with the beam position accordingly, which demonstrates the correlation between them. As the beam position approaches the target lock position, the scatter reaches steady-state. This provides possibility of predicting beam position from scatter measurements. Unlike the ADS system that dithers the test mass, PD measurements is a non-invasive way of monitoring beam position, reducing the potential low-frequency noise in the DARM signal that contains GW information. Since the PD 1 and 4 are located closer to the main beam than PD 2 and 3, their measurements are more sensitive to change of beam position as it moves from point of deviation to the same position (as seen in Figure 13). Thus, much of our focus is put on the PD1 and 4 data.

3.2 Transient scatter in longest stable duration

During the longest stable period in O2 in which the drive align gains of suspensions of PR2 and all test masses are constant, the deviated beam was moved back to the same target positions on the test masses during all of beam alignment processes. Thus, we can analyze the scatter with respect to beam positions, as shown in Figure 16.

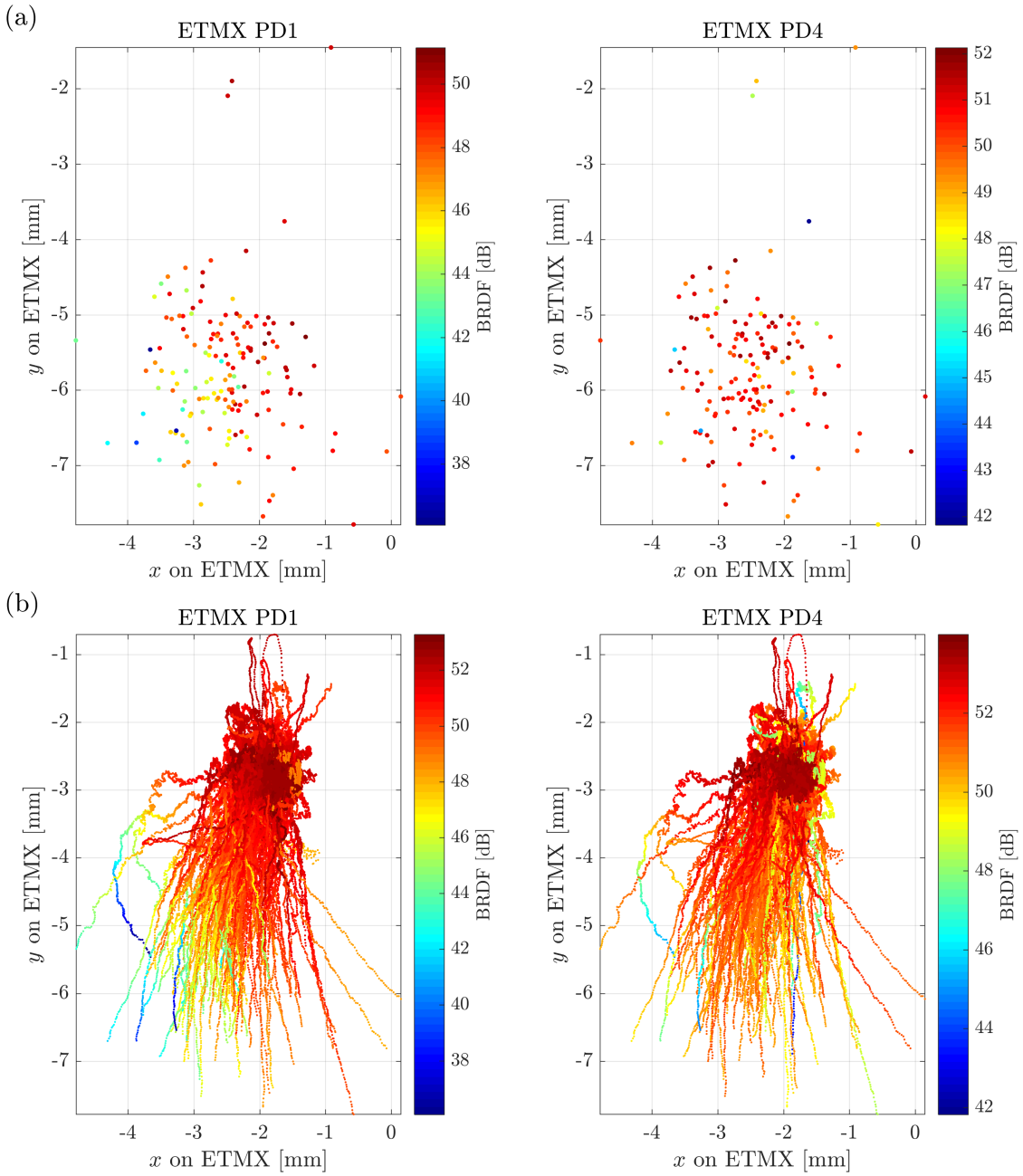

Figure 16: ETMX baffle PD 1/4 measurements at (a) the start and (b) the entire of each beam alignment process. Each trace of scatter represents one alignment process in which deviated beam spot was moved back to the same position of coordinate (-1.8, -3.0) mm.

From the scatter-point plots of ETMX PD, it is seen that clusters of data points at bottom left of ETMX PD 1 share lower BRDF readouts. However, it is difficult to identify any clear trend between BRDF and beam position but the fact that the position on ETMX affects scatter measurements on all eight baffle PD in X-arm (Figure 15). The measured BRDF is not repeatable as its variation easily exceeds 5 dB of our interest at the same beam position in Figure 16 (b). Such variation also pervades in transient scatter of Y-arm in Figure 17.

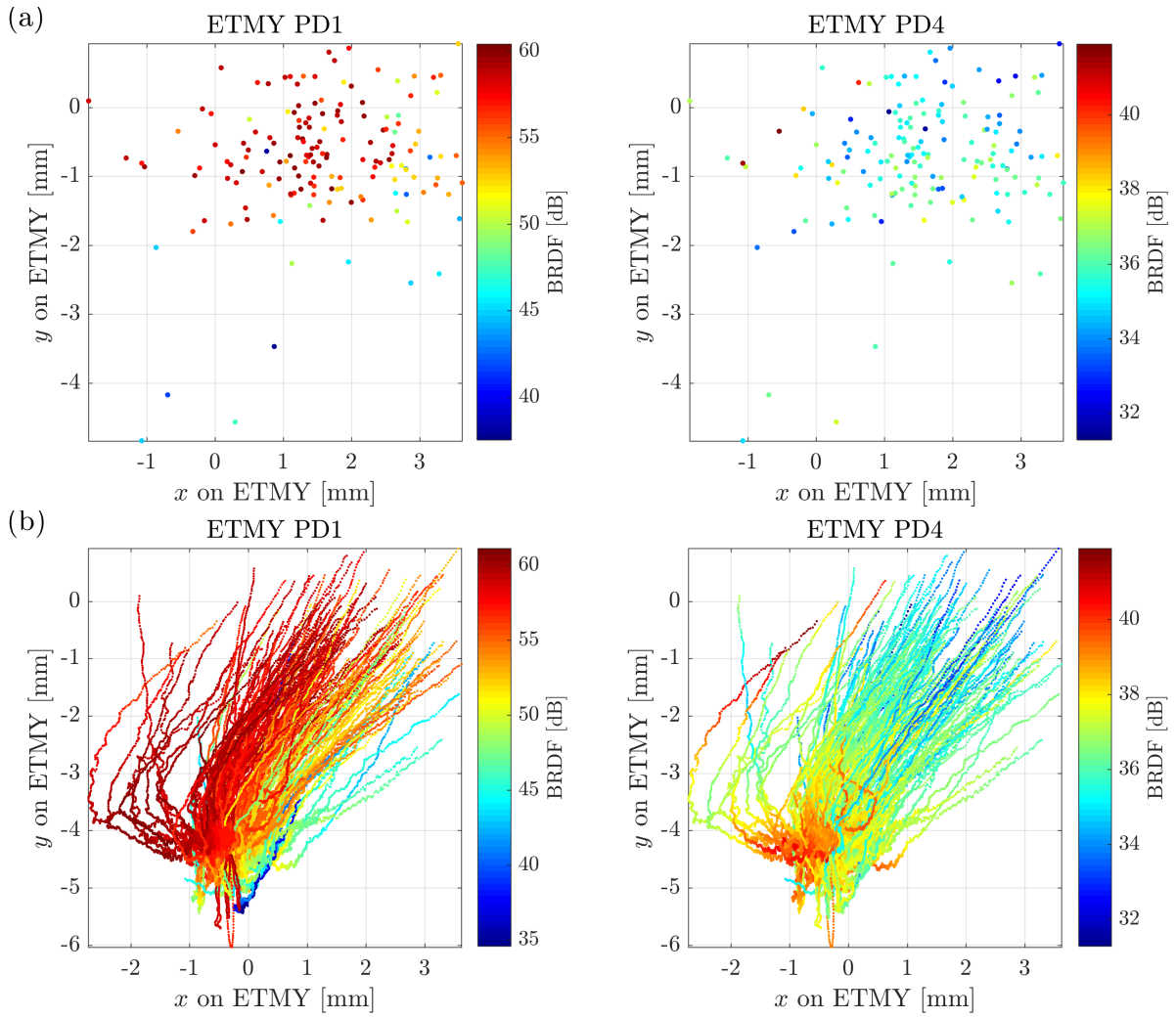

Figure 17: ETMY baffle PD 1/4 measurements at (a) the start and (b) the entire of each beam alignment process. Each trace starts from deviated beam spot to the lock position of coordinate (-0.4, -4.0) mm.

It is also shown that even for very similar beam path, the corresponding scatter trend can be different by a factor up to 20 dB (factor of 10) as in Figure 18.

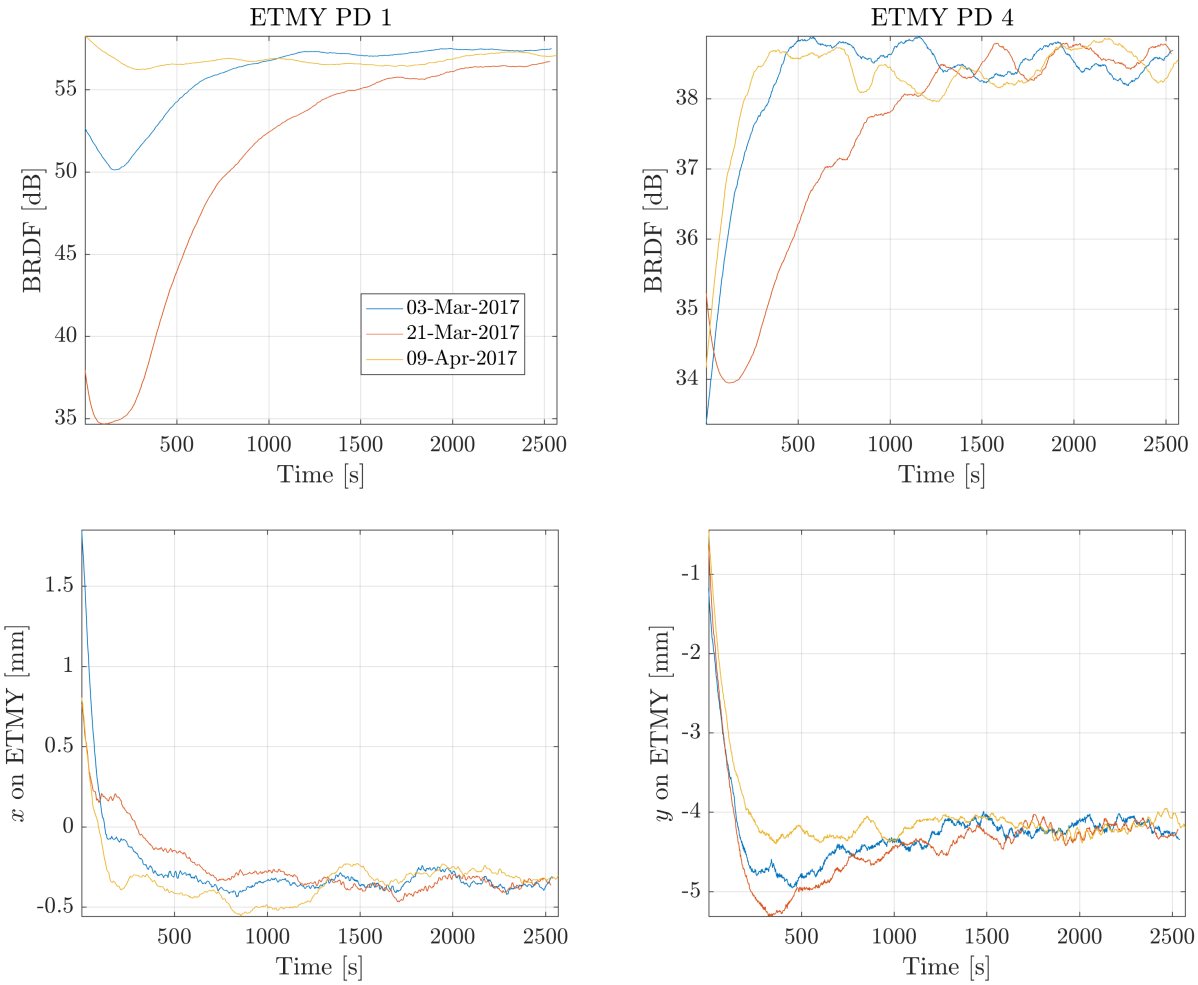

Figure 18: Trends of ETMY PD1 and 4 with respect to ETMY beam position in three alignment processes. All signals are filtered with moving average of 120 seconds

Figure 18 shows three trends of PD responses with similar beam paths. Although all of PD measurement reach the same steady-state value, the variation of initial power measurements of PD1 on Mar. 21 and Apr. 09 are different by a decade (20 dB). Thus, the scatter measured from baffle PD depends on beam positions on both sides of test mass. For SIS, it is capable of simulating the field amplitude distribution with specified tilt of each test mass. Various simulations are done at different beam positions on both ITM and ETM to see their differences, as shown in Figure 19.

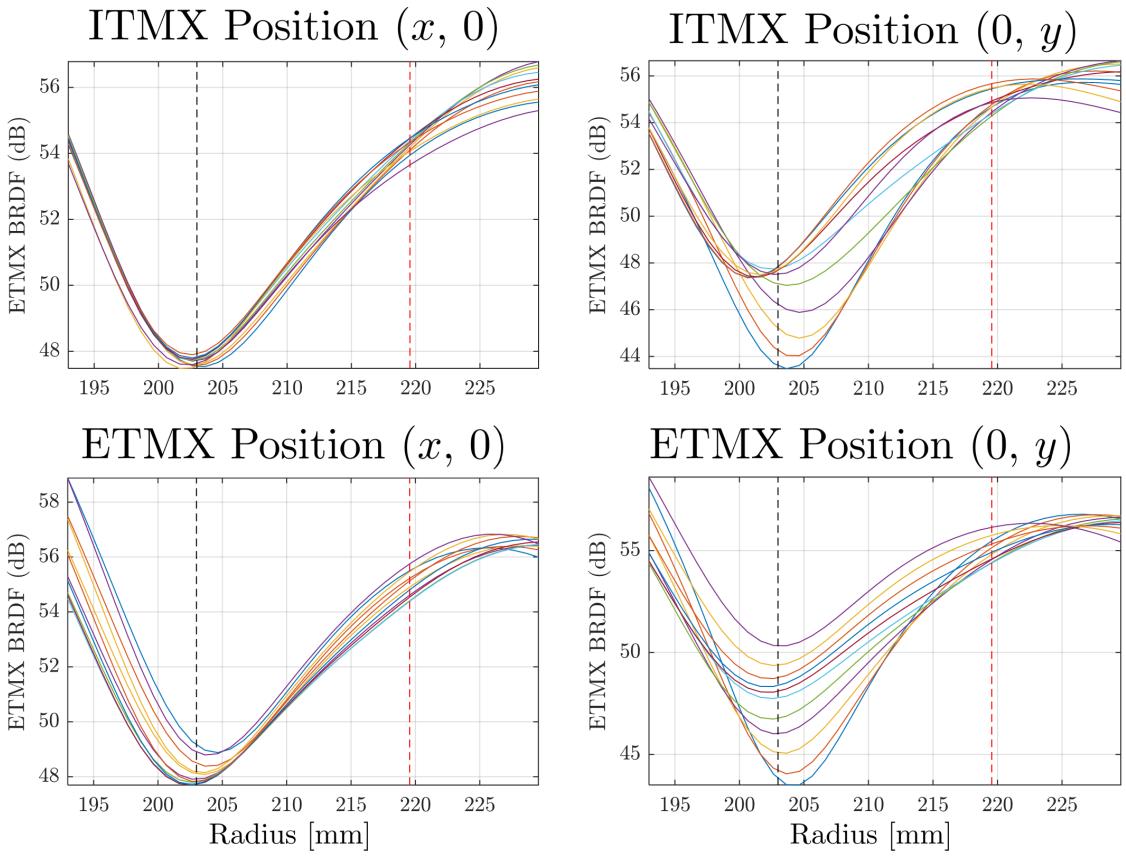

Figure 19: Comparison of SIS of scatter on ETMX given different positions. The variable in the title changes from values -10, -8 ... 10 mm while others are controlled to 0. Each curve in the plot corresponds to one of the values of the variable. The red and black vertical lines indicate the position of PD 1 and 4.

The change of the vertical position on ETMX will result in different profiles with up to 6 dB difference, which is the same change of transient measurements during beam alignment. Using one simulated profile for all predictions is not accurate. It is also very computationally inefficient to simulate every profile for each pair of beam positions on both test masses, and SIS is not reliable at the resolution of decibels. To predict beam position, another model other than SIS is required. Linear regression analysis is hence carried out in the next section to determine relations between PD data and beam positions on ITM and ETM.

4 Regression Analysis

4.1 General linear regression

Extensive regression analytical methods have been developed to characterize correlations between response(s) and predictor(s). Unlike complex nonparametric modelings or neural networks, parametric regression model often can be interpreted as physical implications such as first or higher-order couplings. Among various parametric models, the general linear model is most computationally efficient given the knowledge of structure of the model [11]. A general linear regression models the response y with p-dimensional predictors $x_i, i = 1, 2, ..., p$ as

$$y = \beta_0 + \sum_{i=1}^{K-1} \beta_i f_i(x_1, x_2, ..., x_p) + \varepsilon \tag{9}$$

where β are coefficients of each function f, and ε is the normal distributed random noise. Given n observations, the data can be represented as

$$\mathbf{y} = \mathbf{X}\boldsymbol{\beta} + \boldsymbol{\varepsilon} \tag{10}$$

where $\mathbf{X}$ is the design matrix of $\mathbb{R}^{(n\times K)}$. The best estimate $\mathbf{b}$ of the true coefficients $\boldsymbol{\beta}$ is by ordinary least square estimation. This is the definition of the regression model being linear, as its coefficients can be easily solved as $(\mathbf{X}^{\mathrm{T}}\mathbf{X})^{-1}\mathbf{X}^{\mathrm{T}}\mathbf{y}$. For the univariate model, each row of $\mathbf{X}$ has identical structure. Consider the simple case of independent effects of the parameters with order up to k ($\beta_i = 1$), the design matrix can be represented as

$$\mathbf{X} = \begin{bmatrix} 1 & x_{11} & x_{11}^2 & \dots & x_{11}^k & x_{21} & \dots & x_{21}^k & \dots & x_{p1}^k \\ \vdots & \vdots & \vdots & & \vdots & \vdots & & \vdots & & \vdots \\ 1 & x_{1j} & x_{1j}^2 & \dots & x_{1j}^k & x_{2j} & \dots & x_{2j}^k & \dots & x_{pj}^k \\ \vdots & \vdots & \vdots & & \vdots & \vdots & & \vdots & & \vdots \\ 1 & x_{1n} & x_{1n}^2 & \dots & x_{1n}^k & x_{2n} & \dots & x_{2n}^k & \dots & x_{pn}^k \end{bmatrix} \tag{11}$$

where j is the j^{th} of total n observations. Since the estimated coefficients are always solvable, the terms of design matrix need to be chosen wisely. Another slightly complex design includes the interactions of parameters such as products of polynomials. The j^{th} row of design matrix can be expressed as:

$$\mathbf{X}_j = \begin{bmatrix} 1 & x_{1j} & \dots & x_{1j}^{k_1} x_{2j}^{k_2} ... x_{pj}^{k_p} & \dots & x_{pj}^k \end{bmatrix} \tag{12}$$

where $k_1, k_2 ... k_p \in \{0, 1 ... k\}$ and $\sum_{i=1}^{p} k_i \leqslant k$ are satisfied. Each polynomial term only appears once and k is the upper bound of order of the model. To predict the beam position, we can use four PD on one baffle (4 predictors) or all baffle PD in that arm cavity (8 predictors). However, the complexity increases exponentially with interaction terms added, as shown in Figure 20. For the 8-predictor interaction model with order of 5, its number of terms grows to the order of 10^3, which is impractically high for this application. We will limit our predictors to only four baffle PD, which still has unnecessary terms that have weak effect in the characterization of relationship. Therefore, an algorithm to reduce the dimension is desired for implementation.

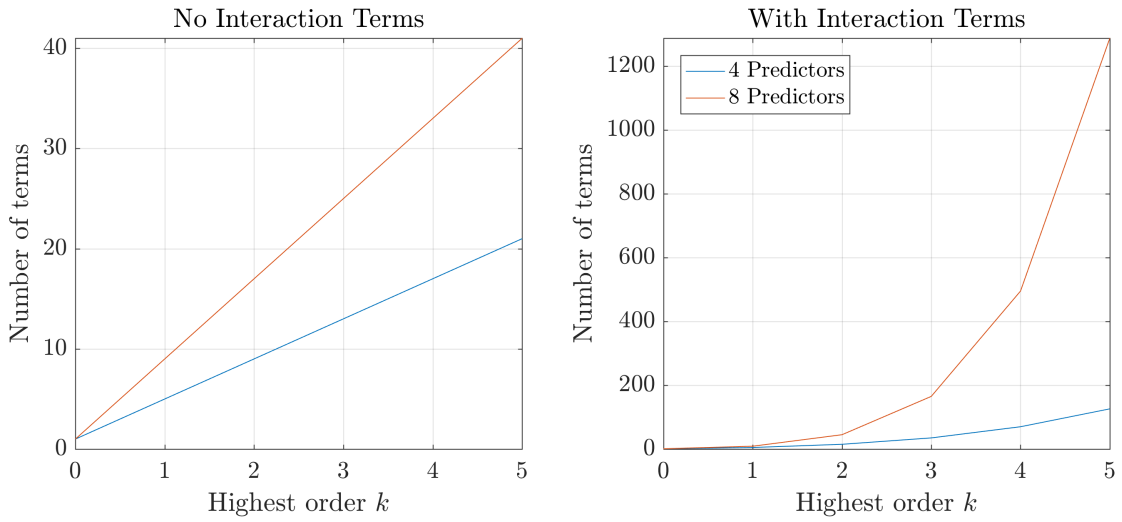

Figure 20: Increment of the number of terms in one row of design matrix with respect to the upper bound order k.

4.2 Stepwise regression

A regression model can always be more accurate on fitting the data set as it gets arbitrarily complex, but its estimation to the future data won't necessarily improve. Since not every order of parameter x_i reveals a strong correlation with response, a stepwise linear regression is performed in practice to add or remove term in the design matrix based on its correlation. Backward stepwise regression is preferred to avoid losing any useful terms and overfitting. To predict the x position on ETMX (response) with four ETMX baffle PD (predictors), the stepwise linear model is trained with all alignment trends of data (size of $\sim 10^6$) in entire O2 for the upper bound of order of 5. The result of training is shown in Figure 22.

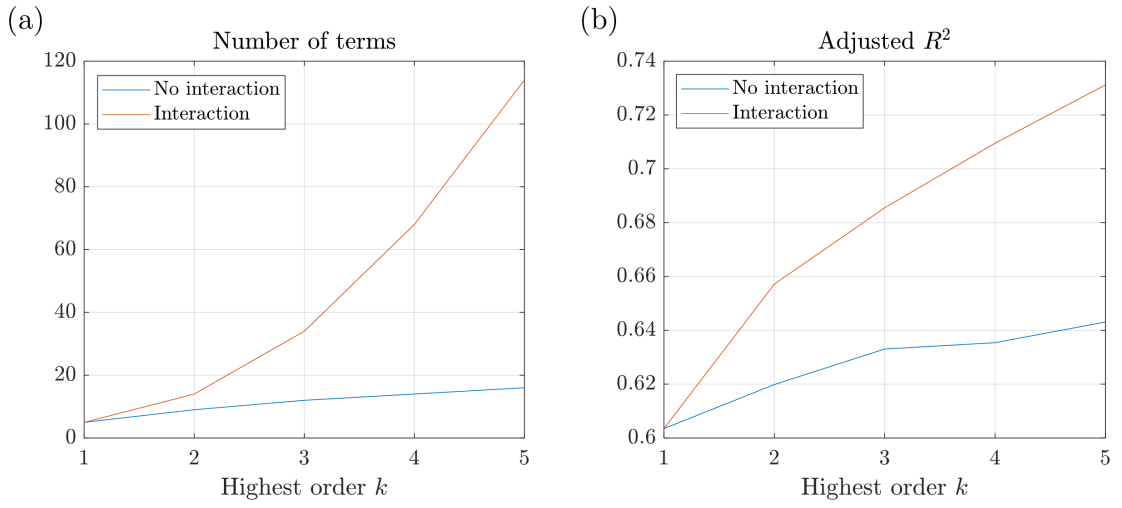

Figure 21: Comparison of (a) the number of terms and (b) the adjusted R^2 between backward stepwise regression on independent and interaction terms.

The new model with interactions reveals a better fitting on the data than mutually independent parameters, given the same order. The reason could be a better design matrix that is closer to the physical correlations between response and predictors, or simply the increased complexity of the model itself. However, both models exhibit latent improvement at higher-order as in Figure 22 (b). The gain in fitting is based on the sacrifice of model simplicity as the number of terms are over 100 after trimming.

To evaluate the degree of overfitting of the model, various criteria have been created. Akaike's Information Criterion (AIC) is a common type of index to measure the complexity of the model, which is given by:

$$\mathrm{AIC} = n \ln \mathrm{SSE} - n \ln n + 2p \tag{13}$$

where SSE is short for Sum of Squared Error, n is the sample size, p is the number of terms of the model. It penalizes the model with large number of predictors. The model with minimum AIC is preferred. The AIC values of the models with highest order of 1 to 5 are shown in Figure 22.

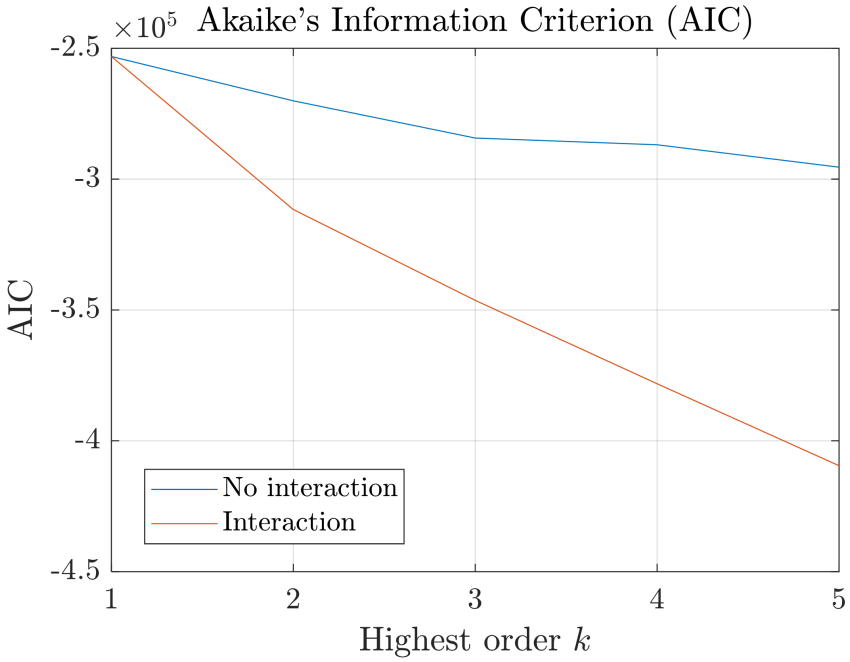

Figure 22: Akaike's Information Criterion (AIC) of the backward stepwise regression composed of independent and interaction terms.

Interestingly, the decreasing trend of AIC is revealed as the upper bound of order grows, implying the positive trade-off between the reduction of SSE with complexity. Thus, it is motivated to train more complex regression models on the data set, and the result is shown in the next section.

4.3 Supervised Learning Model

Supervised machine learning algorithm is an extension of regression analysis and widely used to infer correlations between responses and predictors. It is capable of tackling non-linear relationship by branching decision trees or using an ensemble of regression models. However, it is not as easily interpretable as linear regression models due to its complex algorithm. We trained several common supervised machine learning models with the transient scatter data in the longest stable duration of O2. The goal is to predict the x-position of the main beam on ETMX using four ETMX baffle PD. The result is summarized in the Table 5, including the general linear regression models mentioned previously.

Table 5: Regression models trained with 3-month of transient scatter measurements ($\sim 10^5$ data). RMSE stands for Root-mean squared error, and obs is short for observation. The models are arranged as simple to complex from top to bottom.

Model	R^2	**RMSE**	**Prediction Speed**
5^{th}-order stepwise linear (independent)	0.64	0.17	1.6 $\times 10^6$ obs/sec
5^{th}-order stepwise linear (interaction)	0.73	0.15	1.3 $\times 10^6$ obs/sec
Simple tree ($>$ 32 obs on node)	0.94	0.07	1.7 $\times 10^6$ obs/sec
Complex tree ($>$ 4 obs on node)	0.98	0.04	1.6 $\times 10^6$ obs/sec
Ensemble of Boosted Trees	0.62	0.17	2.2 $\times 10^5$ obs/sec
Ensemble of Bagged Trees	0.99	0.03	6.7 $\times 10^4$ obs/sec

For the three criteria in the Table 5, the best model would have highest R^2 (good fitting), lowest RMSE (less error) and highest prediction speed. As the model gains better prediction, the computational cost rises correspondingly. The top two models, the complex tree and ensemble of bagged trees, exhibit highest R^2 that are almost equal to 1. Complex decision tree consists of branching conditions when a subset of data reveals large error based on one set of model. For the ensemble learning model, it uses multiple regression algorithms to achieve more accurate prediction. Both models would be compared in more detail.

Residual analysis is one useful method to evaluate the quality of the model. Since the regression model assumes normal distribution of the random error, the ideal model would have residuals normally distributed around zero with constant variance and independent of the true value. Figure 23 shows the residual histograms of the top two models.

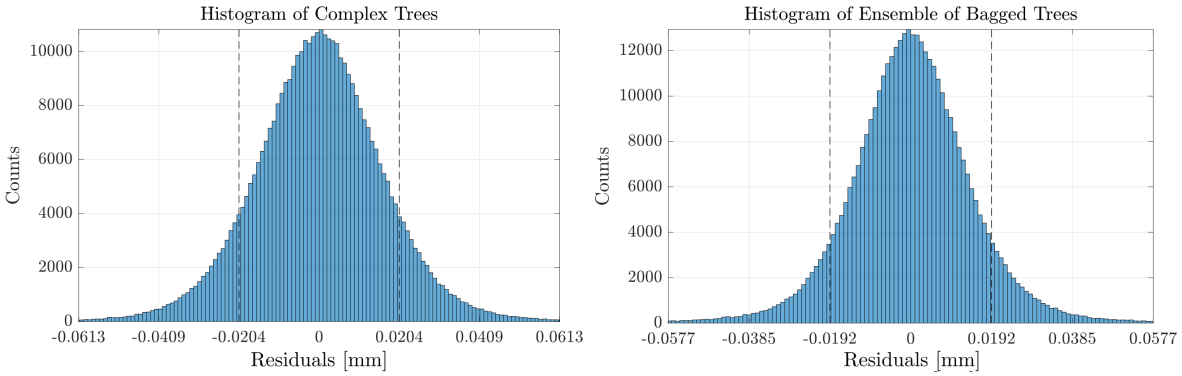

Figure 23: Histogram of residuals of complex tree and ensemble of bagged trees learning models. The values on horizontal axis are multiples of standard deviation of the residuals.

Although the standard deviation of ensemble is smaller than that of complex trees, the difference is as negligible as 6%. The full width at half maximum (FWHM) of the ensemble's Gaussian profile is smaller as well. The distribution of both residuals are shown for more in-detail comparison.

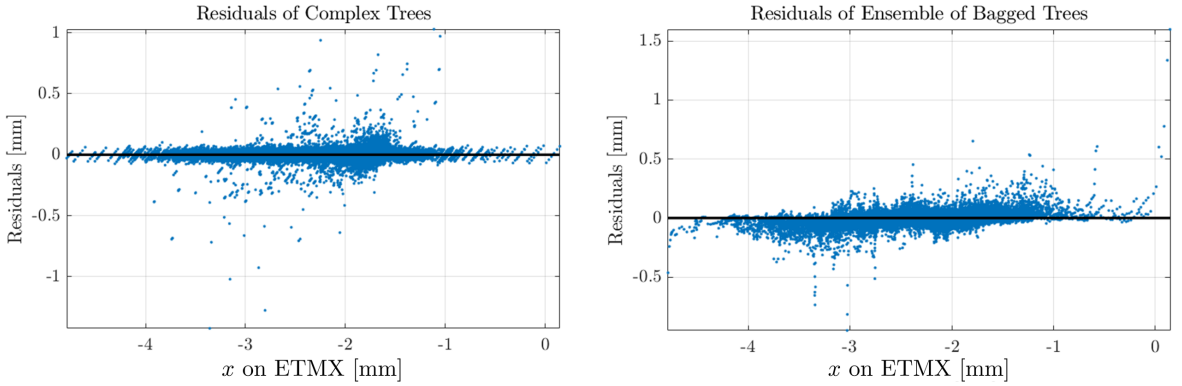

Figure 24: Residual plots of complex tree and ensemble of bagged trees with respect to the response.

In the left plot of complex trees, individual leaf nodes are visible at both ends of the range of the response. The model generates many of such nodes to reduce error at borders of response, where the data is scarce and non-representative. Both residual plots demonstrate nonindependence on the response as the residuals become significantly large at the upper bound of response. Overall, the ensemble of bagged trees algorithm is selected for its accurate and precise prediction and more constant standard deviation through the range of response.

The cross-check of the quality of ensemble model is done by using the first half of training data to predict the last half of data. The first 80 transiences are used to train the ensemble, and the residual of prediction of the last half is collected and shown in Figure 25.

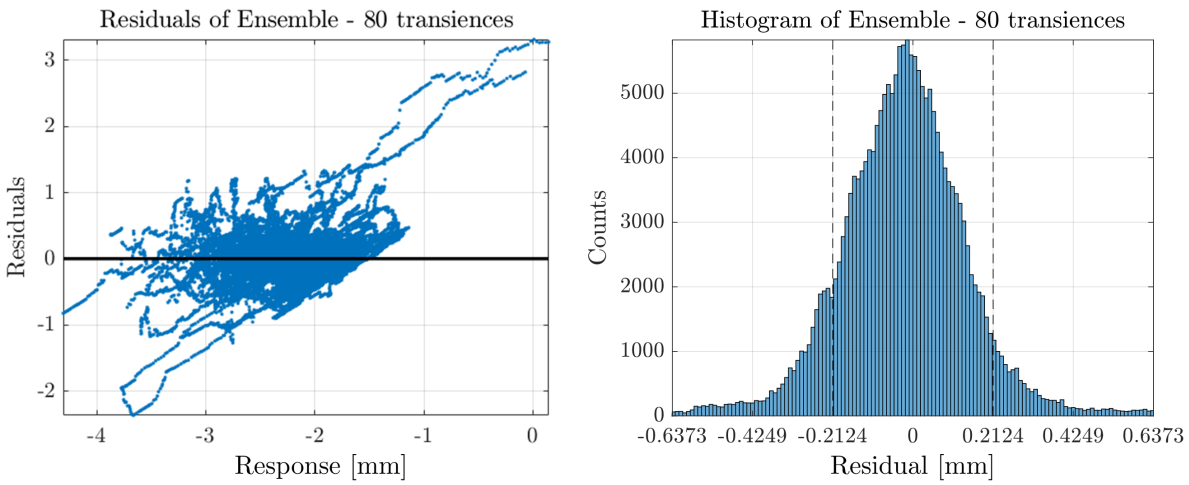

Figure 25: Residual plots of the prediction of the last half of data with ensemble trained by the first half.

The residual distribution is not a normal distribution across the zero, and the variance is not constant for all responses. The three traces on the residual plot that are deviated from the main data, two at the right and one at bottom, are those alignment traces starting from unusual locations in Figure 16. As a result, the standard deviation is roughly 10 times larger than that of model using full data. In reverse, the last half is trained to predict the first half, whose result is in Figure 26.

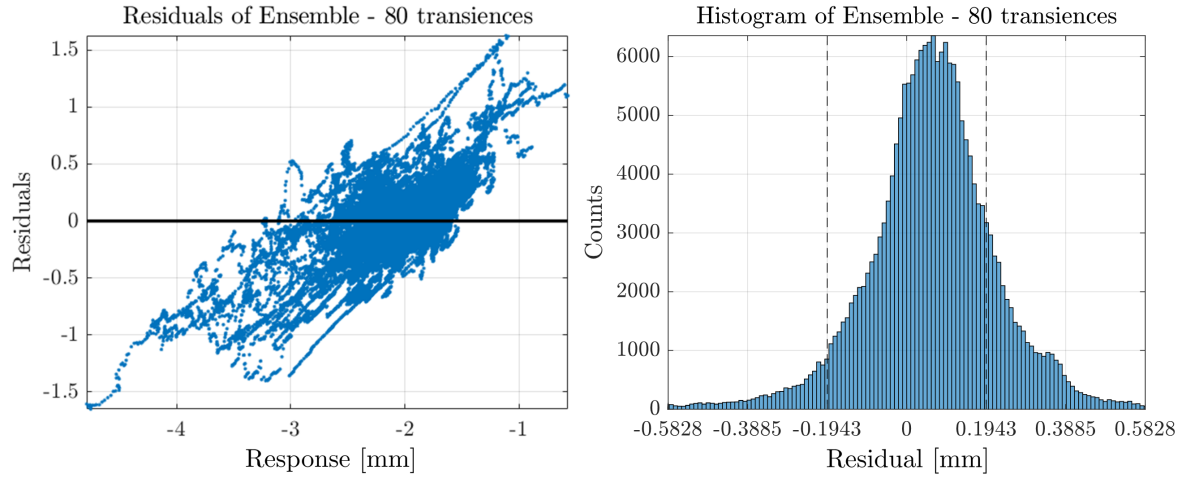

Figure 26: Residual plots of the prediction of the first half of data with ensemble trained by the last half.

When it is done in reverse, the residual distribution has less deviated points, since the unusual alignment path is trained in the model. However, the residual indicates a slight bias of around 0.05 mm from zero, as seen in the right plot of Figure 26. The reason is that most of the trace in the last half do not cover the range of them in the first half. A training data

set covering wide range is much more desired to avoid bias. The alignment traces of the entire O2 is expected to cover a larger range, as shown in Figure 27.

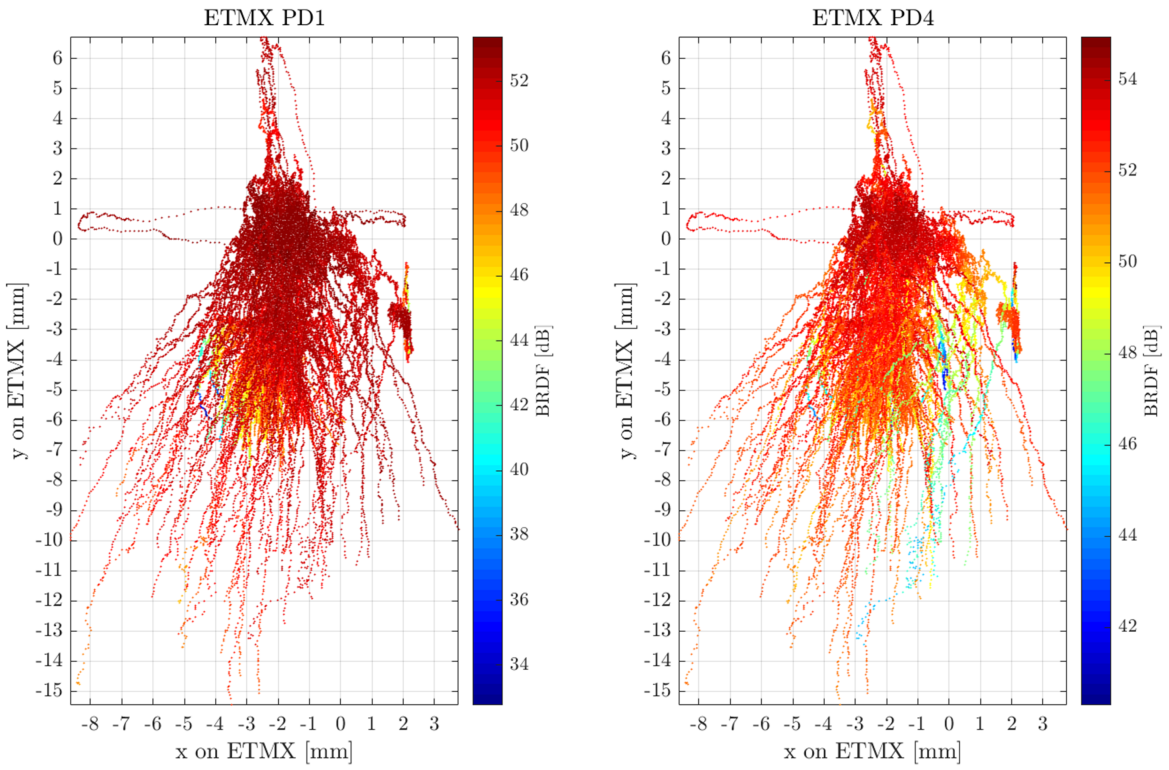

(a) ETMX PD 1 and 4 measurements during all alignments on ETMX

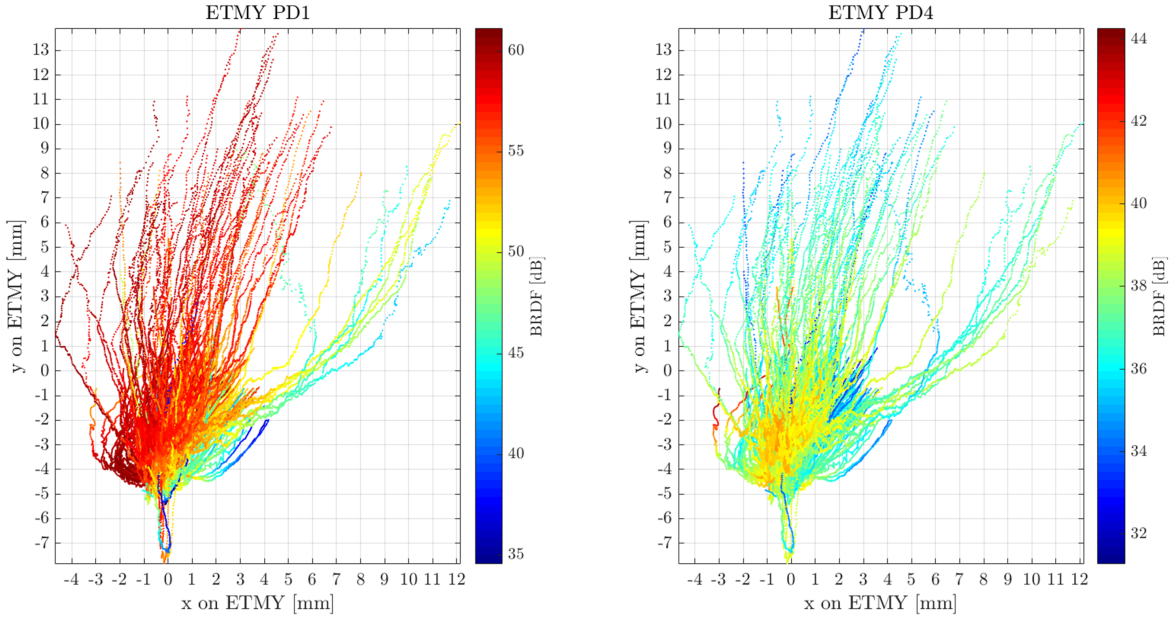

(b) ETMY PD 1 and 4 measurements during all alignments on ETMY

Figure 27: ETM baffle PD 1 and 4 measurements with respect to beam positions on ETM. Traces represent alignment paths in the entire O2.

Both data set have well-covered area of 5-mm circle and a few stretches to the location far from origin. The ensemble of bagged trees learning is done on this data with size of 1.6 million, as shown below.

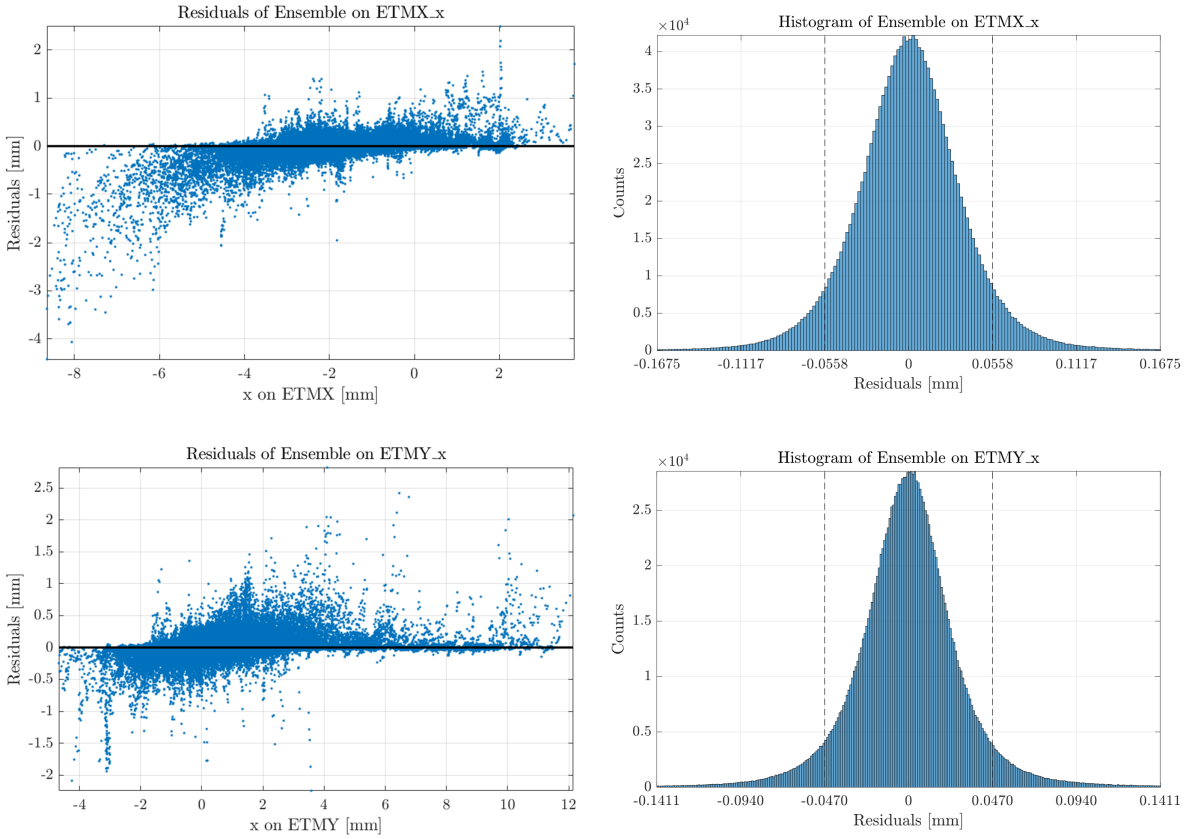

Figure 28: Residual plots of the ensemble model trained with all transient scatter in O2.

It is seen that the standard deviation of residual is constant of around 0.05 mm in around 5-mm interval. Both residual plots still demonstrate strong nonconstancy of variance with high variance at extrema values in the response range. With more diverse data set, the estimation bias can be reduced and the model is less susceptible to unusual data like an alignment path from an unfamiliar start point.

5 Conclusion & Future Work

In this report, we compare the optical scatter measured in the FP cavity of LLO thoughout O2 locks with the semi-quantitative SIS simulation. The measurements match with the prediction within 10 decibel. The coupling between scatter and beam position is studied with measurements during the beam alignment process before each lock. Various regression models are tested to predict beam position on the scale of millimeter from scatter ranging in a few decibel. Using the ensemble of bagged trees supervised machine learning algorithm, the model is trained with four ETM baffle PD and capable of predicting beam position on ETM with $\sigma < 0.1$ mm. All of the work is done on MATLAB, and the well-commented software can be found in the LIGO-T1800224-v0.

The future work includes more refinement of hyperparameter tuning of the model to reduce the nonindependence of residual and its nonconstancy variance. The regression with 8 predictors (all baffle PD in cavity) could be tested to compare its advantage with current 4-predictor model. In O3, the ETM will be replaced to reduce the spiral pattern shown in Figure 8. The simulation of beam profiles in O3 are shown in the Figure 29.

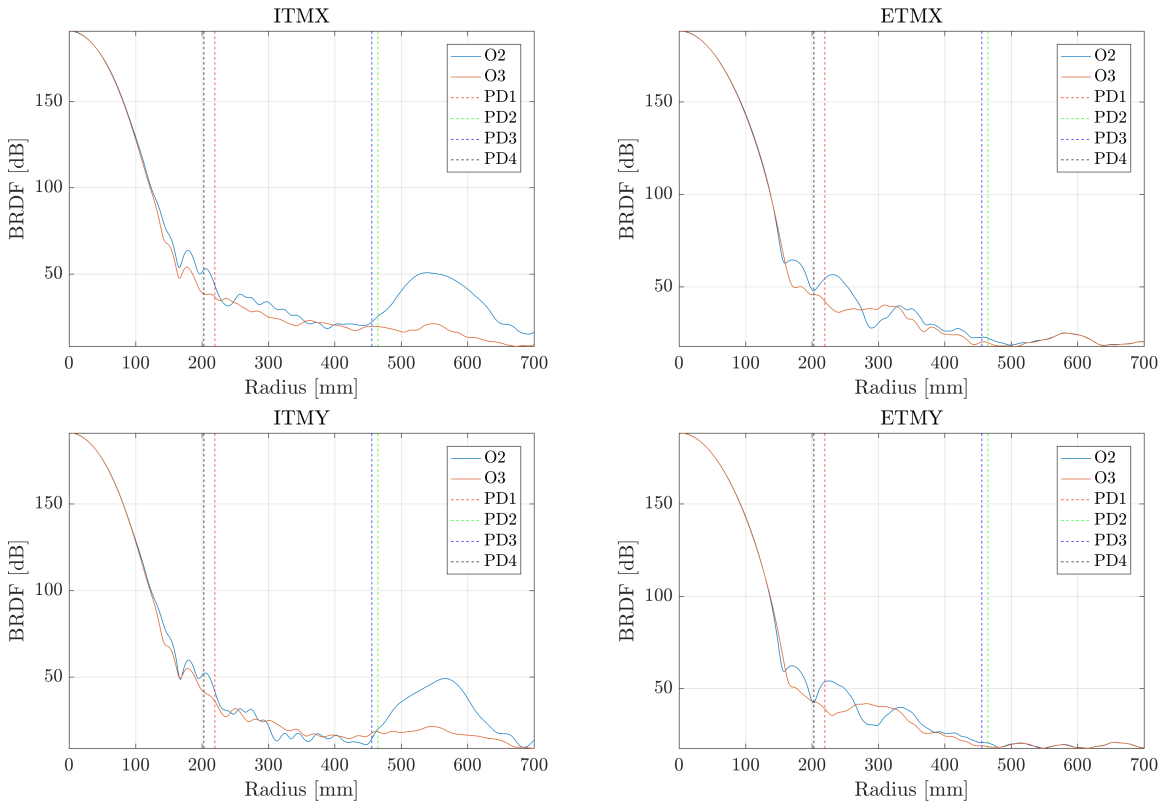

Figure 29: Field profiled on LLO baffles in O2 and O3.

Clearly, the spiral pattern at radius range of 500 to 600 mm is suppressed in the new test mass. It is interesting to see the improvement by measuring the new scatter predicted in Figure 30.

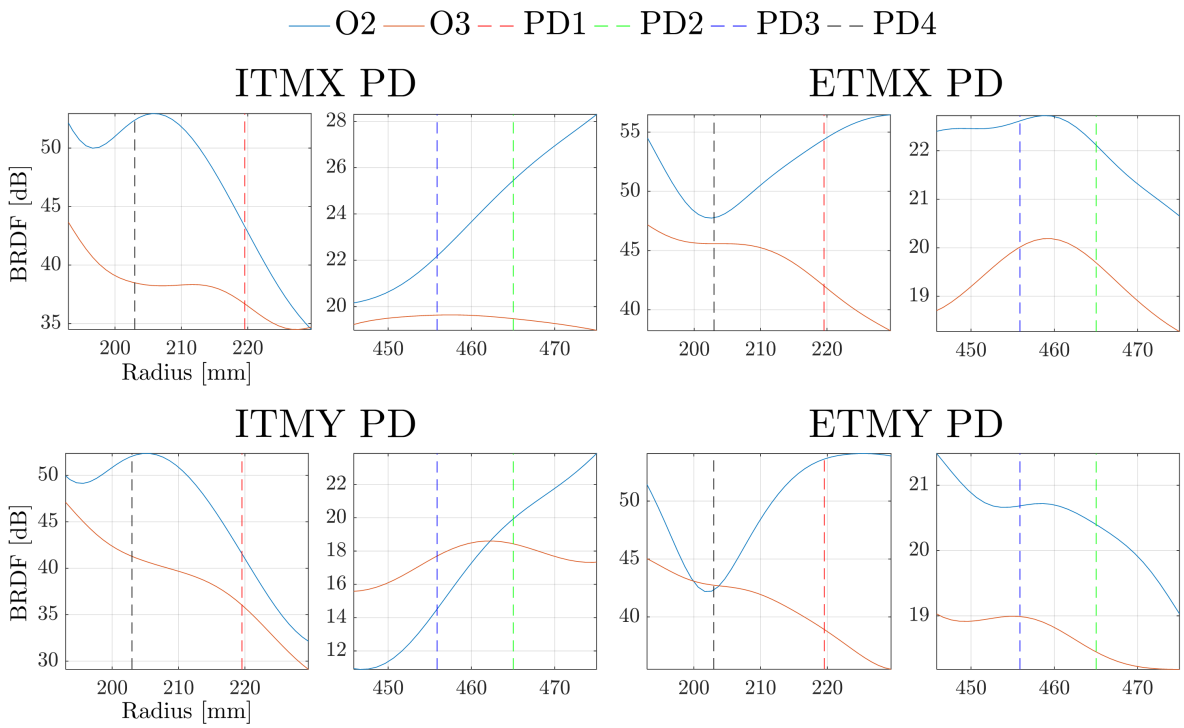

Figure 30: Comparison of arm cavity baffle PD measurements of LLO between O2 and O3.

Before O3, we can map the main beam thoroughly on the ETM to obtain the training data. Then the regression model can be implemented to measure beam position and hopefully integrated to replace the current dither-based system.

Acknowledgment

The author is very grateful to Anamaria Effler and Valera Frolov for their patient mentoring as well as Hiro Yamamoto for his consistent help on SIS! The author also appreciates Marie Kasprzack, Arnaud Pele, Carl Blair, Joe Betzwieser, Corey Austin, Keith Thorne and all other LLO fellows for answering all types of questions and offering constructive insights. A million thanks to California Institute of Technology and National Science Foundation for providing such an unforgettable research experience.

References

[1] R. Adhikari, *Gravitational radiation detection with laser interferometry*. Rev. Mod. Phys. 86, 121 (2014).

[2] P. Saulson, *Interferometric Gravitational Wave Detectors, 2nd Edition*. Section 6.6 pp. 99 (2017).

[3] H. Rew and J. Betzwieser, *Modeling of Optical Scattering in Advanced LIGO*. LIGO DCC P1400197.

[4] H. Yamamoto, *SIS (Stationary Interferometer Simulation) manual*. LIGO-T070039-v8.

[5] G. Billingsley, *ITM04 Figure Measurement*. LIGO-E1200265-v3.

[6] G. Billingsley, *ETM07 Figure Measurement*. LIGO-E1300365-v1.

[7] The LIGO Scientific Collaboration, *Advanced LIGO*. Class. Quantum Grav. 32 074001 (2015).

[8] Excelitas Technology, *YAG Quadrant Datasheet*. http://www.excelitas.com/Downloads/DTS_YAG-quadrants.pdf.

[9] J. Chavez and E. Sanchez, *AdvLIGO SUS BSC5-L1, XYZ Local CS for SLC Arm Cavity Baffle*. LIGO-D1200677-v1.

[10] J. Goodman, *Introduction to Fourier Optics, 2nd Edition*. Chapter 2-4

[11] J. Rawlings, et al. *Applied Regression Analysis: A Research Tool, Second Edition*. pp. 250.

Appendix A Fabry-Pérot Cavity

The FP cavity is composed of two HR-coated mirrors vertically aligned with each other. A simple cavity that has mirrors with transmittance t_1^2, t_2^2 and reflectance r_1^2, r_2^2 is shown in Figure 31

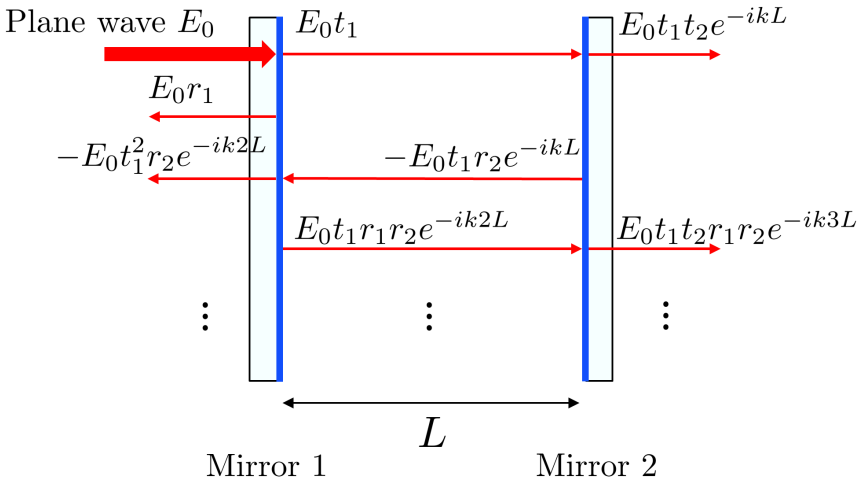

Figure 31: Configuration of the simple FP cavity. The blue layer on the mirror is the HR surface.

A plane wave of E_0 is incident on the left mirror and reflected back with amplitude $E_0 r_1$. The rest transmits through and then interacts with the second mirror. The field in the cavity bounces back and forth with decaying amplitude and increasing phase. Summing the reflected field, we obtain:

$$\begin{aligned} E_{\text{refl}} &= E_0 r_1 - E_0 t_1^2 r_2 e^{-i2kL} \sum_{n=0}^{\infty} \left(r_1 r_2 e^{-i2kL}\right)^n \\ &= E_0 \left(\frac{r_1 - r_2(t_1^2 + r_1^2) e^{-ik2L}}{1 - r_1 r_2 e^{-ik2L}} \right) \end{aligned} \tag{14}$$

Similarly, take the sum of transmitted fields:

$$\begin{aligned} E_{\text{tran}} &= E_0 t_1 t_2 e^{-ikL} \sum_{n=0}^{\infty} \left(r_1 r_2 e^{-i2kL}\right)^n \\ &= E_0 \left(\frac{t_1 t_2 e^{-ikL}}{1 - r_1 r_2 e^{-ik2L}} \right) \end{aligned} \tag{15}$$

Taking the square of the modulus of the field to get the intensity:

$$P_{\text{refl}} = |E_{\text{refl}}|^2 = E_0^2 R_{\text{FP}} \tag{16}$$

$$P_{\text{tran}} = |E_{\text{tran}}|^2 = E_0^2 T_{\text{FP}} \tag{17}$$

and

$$T_{\mathrm{FP}} + R_{\mathrm{FP}} = 1 \tag{18}$$

The energy is conserved. Assume the mirrors are identical with $r_1 = r_2 = \sqrt{R}$, the expressions of the transmittance and reflectance of the FP cavity are:

$$R_{\mathrm{FP}} = \frac{2R(1-\cos 2kL)}{1+R^2-2R\cos 2kL} \tag{19}$$

$$T_{\mathrm{FP}} = \frac{(1-R)^2}{1+R^2-2R\cos 2kL} \tag{20}$$

As the length of cavity approaches the multiple of wavelegnth ($L = n\lambda = 2n\pi/k, n \in \mathbb{N}$), the reflectance would approach zero. The mirror reflectance R would affect the sensitivity of R_{FP} and T_{FP} with respect to cavity length, as shown in Figure 32.

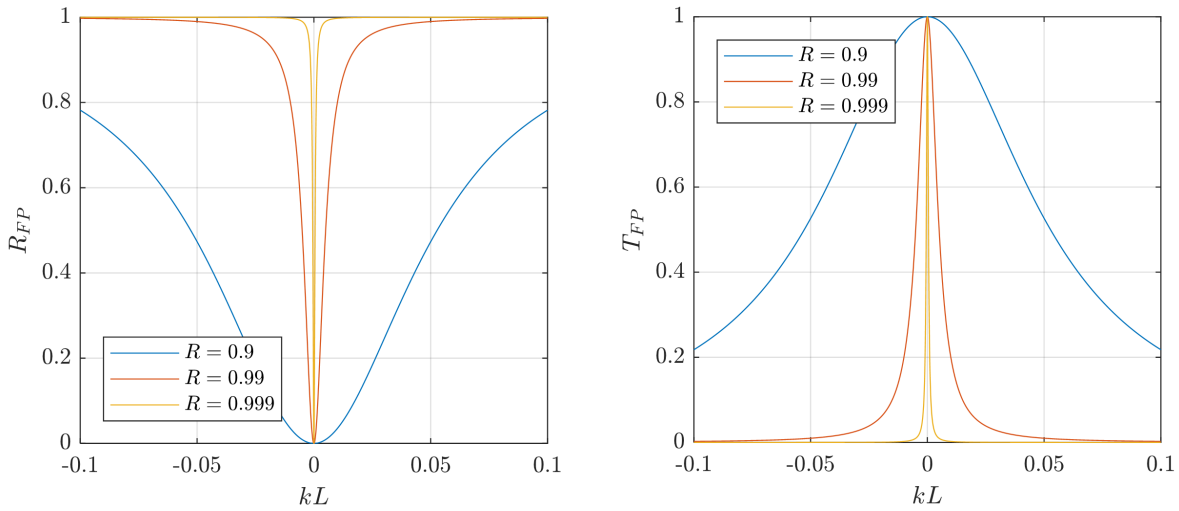

Figure 32: Reflectance and transmittance of FP as a function of cavity length under various reflectance of mirror.

The higher the mirror reflectance R is, the more sensitive the cavity would be to the cavity length, which satisfies the need of LIGO to detect infinitesimal change of length. In aLIGO, the transmittance of ITM is 0.014 and that of ETM is 5 ppm, leading to the high finesse of the FP cavity.

Appendix B Cross-calibration of Photodiode

During the O2, the test masses in the FP cavity was occasionally misaligned from facing to each other and failed to form resonance. The main beam was then centered back to the correct position by yawing or pitching the test masses. To determine the correct yaw & pitch gains of ETM, the green laser (532 nm) located at the back of ETM was directed to the PD 1 and 4 on ITM baffle respectively by changing ETM attitude, and then the average of the separate gains would center the main beam on ITM (Figure 33 (a)). Similarly, the ITM yaw & pitch can be determined by averaging gains that point laser beam at the PD 1 and 4 of ETM baffle, as shown in Figure 33 (b). The PD 1 and 4 measurements during beam centering can be used to find the variance between them. The beam centering process

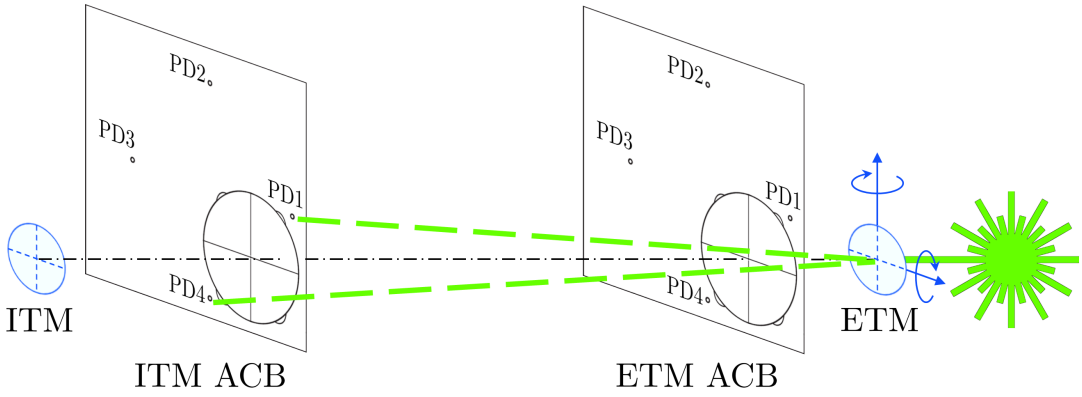

(a) Centering main beam on ITM by ETM yaw & pitch

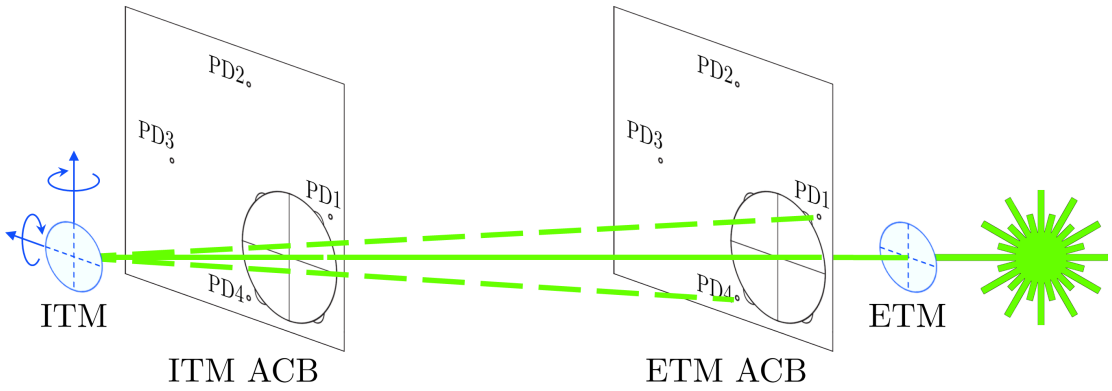

(b) Centering main beam on ETM by ITM yaw & pitch

Figure 33: Schematics of the beam centering process, during which the PD 1 and 4 are shined directly by the same source

can be found when *L1:GRD-ISC_LOCK_STATE_N* equals to 9. The raw data of PD 1 and 4 measurements at the first three and last three times of centering process through O2 are found to compute the variance, an example of ITMX PD as shown in Figure 34.

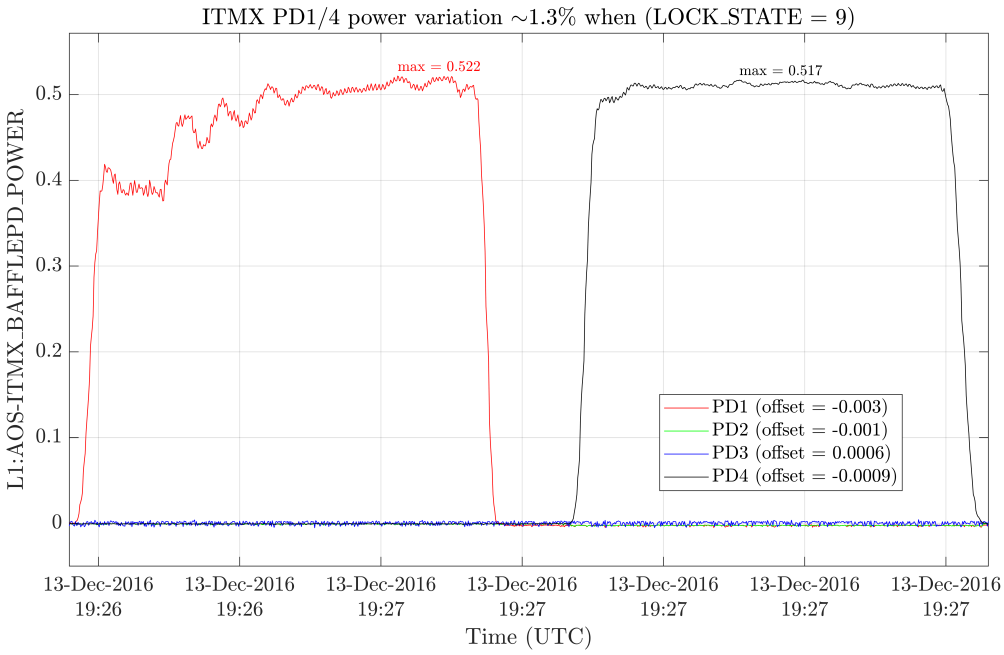

Figure 34: Time series of ITMX baffle PD 1 and 4 measurements during the first beam centering. Each grid is 10 seconds.

It is seen that the PD 1 was under green beam for 20 seconds until its power reaches maximum, and then it was repeated on PD 4. In contrast, the other two PD (2 and 3) were not receiving any light and stayed null. The calibration results for all baffles during the six beam centering processes are summarized in Table 6.

Table 6: Variance of PD 1 and 4 on all arm cavity baffles measured at first and last three times of main beam centering

Time	**ITMX**	**ETMX**	**ITMY**	**ETMY**
Dec. 13, 2016	1.3%	2.1%	2.9%	0.9%
Dec. 19, 2016	3.7%	1.9%	1.1%	1.0%
Dec. 21, 2016	4.1%	2.2%	0.9%	1.6%
Jul. 31, 2017	4.0%	2.0%	2.5%	0.9%
Aug. 5, 2017	4.1%	2.0%	3.4%	1.1%
Aug. 22, 2017	4.4%	1.8%	2.0%	0.8%

The variance of PD 1 and PD 4 at all baffles can be concluded as $2\% \pm 1\%$. Assume that the response of PD is the same for both green and IR laser (1064 nm), the variance of PD 1 and 4 is negligible and much less than the uncertainties caused by fluctuating environmental effects.

Appendix C Scatter in LIGO Hanford Observatory

The LIGO Hanford Observatory (LHO) is the twin detector of LLO, and they operate simultaneously to reduce probability of false positive of detection of GW. Both detectors have identical design, so it is interesting to analyze and compare the scatter of LHO with that of LLO in O2, as shown in Figure 35.

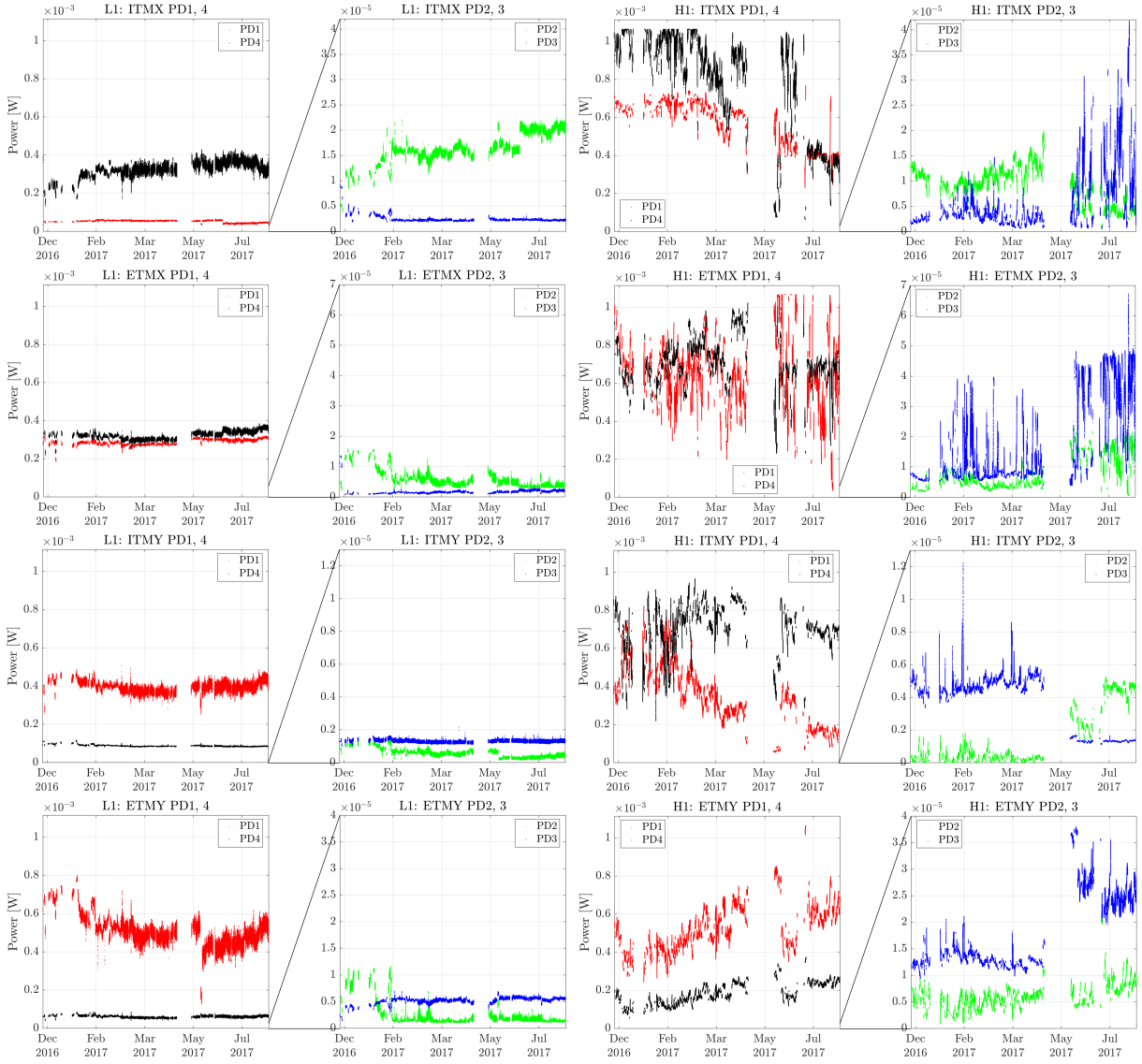

Figure 35: Scatter power measured by arm cavity baffle PD in LLO and LHO throughout O2. Note the color red, green, blue, black (RGBK) represent PD 1-4 respectively.

The LHO PD are generally measuring higher scatter power that saturates the photodiode of ITMX PD 4 and ETMX PD 1, but the measurements are less stable than LLO. The primary reason is that the lock beam positions were not fixed in LHO due to the lack of alignment dither system, as in Figure 36.

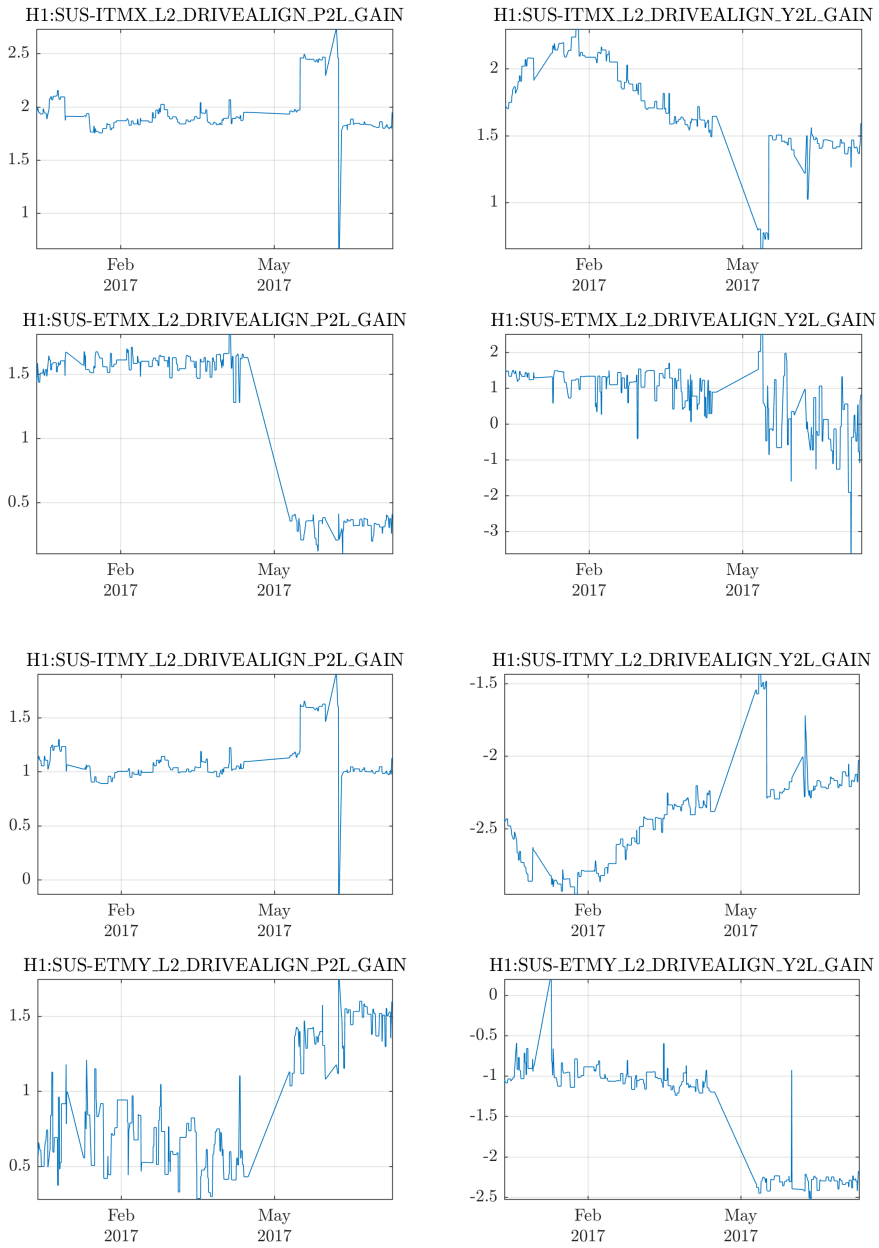

Figure 36: Requested gains that control the beam position on test mass in LHO. The P2L is pitch to length and Y2L is yaw to length, respectively.

With the knowledge of the cavity power in O2, the BRDF of scatter can be obtained and compared with simulation. The coupling between scatter BRDF and steady-state beam position can be used to train regression model and predict future beam positions.